2019

The Weak Nuclear Form Factor: Nuclear Structure & Coherent Elastic Neutrino-Nucleus Scattering

Jesse A. (Jesse Antonio) Hernandez

FLORIDA STATE UNIVERSITY

COLLEGE OF ARTS AND SCIENCES

THE WEAK NUCLEAR FORM FACTOR:

NUCLEAR STRUCTURE & COHERENT ELASTIC NEUTRINO-NUCLEUS SCATTERING

By

JESSE A. HERNÁNDEZ

A Thesis submitted to the
Department of Physics
in partial fulfillment of the
requirements for the degree of
Master of Science

2019

Jesse A. Hernández defended this thesis on August 13, 2019.
The members of the supervisory committee were:

Jorge Piekarewicz

Professor Directing Thesis

Simon Capstick

Committee Member

Ingo Ludwig Wiedenhoever

Committee Member

The Graduate School has verified and approved the above-named committee members, and certifies that the thesis has been approved in accordance with university requirements.

For my mother; without your immeasurable sacrifices and always encouraging me to reach for the stars, this would have never been possible.

TABLE OF CONTENTS

LIST OF TABLES

LIST OF FIGURES

ABSTRACT

The weak nuclear form factor is the final missing piece to complete our understanding of the structure of atomic nuclei and the Coherent Elastic Neutrino Nucleus Scattering (CEνNS) cross section. The weak form factor is dominated by the neutron distributions of the atomic nucleus, which are poorly known. The complex scalar and vector potentials within the nucleus are provided using a Relativistic Mean Field (RMF) approach. These potentials are used to calculate the point neutron and proton distributions, and in conjunction with single-nucleon electric Sachs form factors—obtained from data—are used to predict the weak form factor. It is determined that the radius of the proton distributions agree within 1% to the experimental values. The agreement of the proton distributions gives confidence that the predicted neutron distributions are computed correctly. It is also determined that to constrain the weak form factor, next-generation measurements need to be at $\leq 1\%$ error. The reduction to the CEνNS cross-section due to the weak form factor at small momentum transfer is determined to be between $\sim 10-40\%$ for neutron number, N, ranging from 20 to 126. The findings show that the precise measurement of the weak form factor is necessary for the accurate determination of the CEνNS cross section and our comprehension of the nuclear structure as a whole, namely understanding the neutron distributions. Most importantly, the predicted quantities and estimated errors give guidance to experiments measuring the weak form factor.

CHAPTER 1

INTRODUCTION

1.1 Brief History

The weak neutral current was discovered in 1973 by the first observation of neutrino and electron scattering [4]. In the following year, Daniel Freedman proposed a coherent neutrino interaction with nuclei [5] that began a forty-three year journey to discovery. The discovery of the weak neutral current meant that now there was a channel for the quarks to couple with a neutral weak boson, namely the Z, and in its theoretical description implied the coherent coupling to all nucleons within the atomic nucleus. The coherent coupling is only valid in the limit that the momentum transfer is much smaller than the inverse of the nuclear radius, i.e., $q \ll R^{-1}$. As aforementioned, the forty-three year journey would culminate in a discovery in 2017 by COHERENT collaboration at The Spallation Neutron Source at Oak Ridge National Lab using sodium doped cesium iodine (CsI[Na]) [6]. The coherent neutrino interaction is now called Coherent Elastic Neutrino Nucleus Scattering (CEνNS).

Due to the weak nature of the interaction, CEνNS cross section is enhanced by the number of neutrons squared (i.e., $\sim N^2$) [7] and thus has a comparatively large cross section at similar energies to other neutrino processes. The enhancement due to the number of neutrons in the target nucleus and the relative strength of the cross section compared to other neutrino processes are illustrated in Figure 1.1. The enhancement due to CEνNS will be shown in Section 2.1. However, Freedman described his 1974 paper as "...an act of hubris ..." because of the "...grave experimental difficulties..." [5]. The difficulty of measuring CEνNS in a lab stems from the ability to measure the astronomically small recoil of the nucleus (i.e., few keV) scattering off low energy neutrinos. The driving force that allowed the first measurement of CEνNS has been the search for dark matter. For direct detection of dark matter the kinematics must be reconstructed from a small nuclear recoil. Consequently, detectors that could measure nuclear recoils at the necessarily small energies

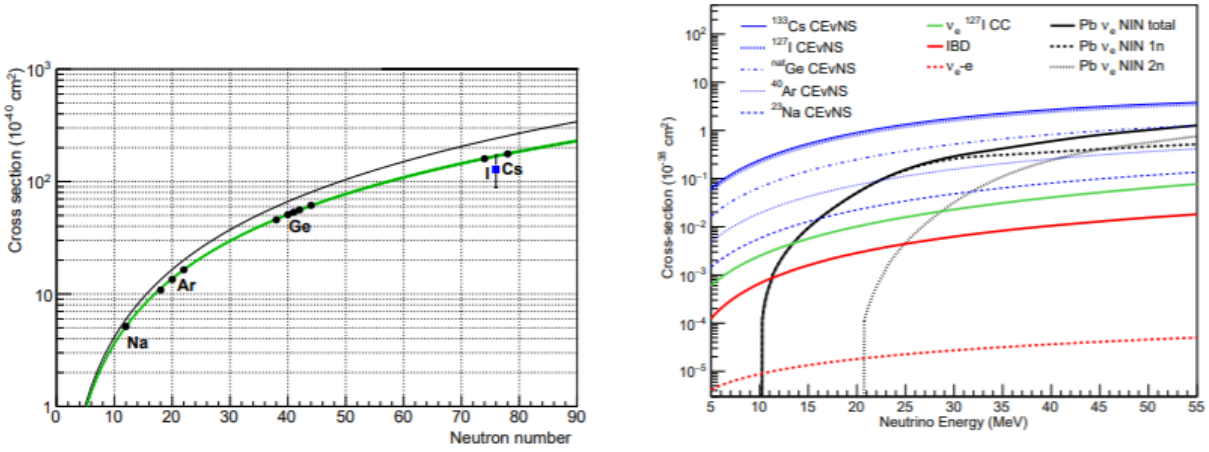

Figure 1.1: (color online) (**Left**) Illustrates the $\sim N^2$ behavior of the CEνNS cross section. (**Right**) Illustrates the enhancement of the CEνNS process over other neutrino processes: neutrino induced neutron (NIN), charged current (CC), inverse beta decay (IBD), etc. Figure from [1].

were developed. The direct detection of dark matter is exactly analogous to the detection of CEνNS due to the fact that the outgoing neutrinos cannot be measured and the incoming neutrino spectra is well known in the Standard Model (SM) framework. It is evident that in the years to come CEνNS will be measured further with extreme precision due to these innovations.

1.2 Motivations

In 1930, Wolfgang Pauli wrote a letter describing a new particle resulting in the theory of β-decay six years later by Enrico Fermi [8]. Evidently, the elusive, minuscule fundamental particle (i.e., the neutrino) has played and continues to play a vital role in our scientific theories. The neutrinos involved in CEνNS makes this reaction extremely robust and important to study for the advancements of our fundamental understanding of the universe. Some of the most enticing aspects of CEνNS are: the enhancement in the cross section, the fact that it is flavor blind—all known generations of neutrinos are indistinguishable—and the method of observation using the recoil of a nucleus. As a result, CEνNS is extremely valuable to test

the SM of particle physics as well as non-standard interactions (NSI), properties of nuclei in nuclear physics with broad applications in astrophysics, and becomes necessary for the search for dark matter in our universe.

1.2.1 Nuclear Physics

The goal of nuclear physics is to comprehend the properties of nuclear matter and the diverse nature of its structure. To achieve these fundamental goals nuclear physicists are leading the charge to find the equation of state (EOS) of nuclear matter and are precisely tuning the interactions within the nucleus to understand its finite structure.

Much progress has been made to understand the fundamental structure of the proton distribution within the nucleus through electron scattering experiments, analysis of muon spectra and other methods [9]. On the contrary, the neutron distributions are poorly known and are required to fully begin understanding the entirety of the nuclear structure. Efforts to extract the neutron distributions from proton nucleus scattering data [10, 11, 12, 13] have been shown to have large model-dependent uncertainties on the order of 10% [14]. Only within the past couple of decades have powerful methods for analyzing the neutron structure in a model-independent way, been accomplished. These efforts have been made with parity violating (PV) electron scattering experiments where the weak sector can be measured directly [15]. PV electron scattering had recently been used to measure the radius of the neutron distribution of Lead-208 [3, 16]. The parity violating asymmetry—the asymmetry of left and right handed electron cross sections—has been shown to be sensitive to the neutron radius [17]. Although, PV electron scattering experiments have proven to be a powerful tool, measuring the small asymmetry is difficult and the experimental uncertainties need to be refined. With that being said, CEνNS is a purely weak mediated interaction and due to the fact that it has a relatively large cross section for a neutrino process at low energy, it gives the best opportunity for an entirely model-independent measurement of the neutron density distribution and weak form factor [14, 18].

In turn, a precise measurement of the radius of the neutron density distribution would help further constrain the EOS of nuclear matter. The EOS describes the relation between

pressure, density, and temperature of nuclear matter; it is also necessary to extract many properties of nuclei. The EOS of cold nuclear matter can be approximated to lowest order to be the sum of the energy per nucleon of symmetric and asymmetric nuclear matter [19],

$$E(\rho, \alpha) = E_0(\rho, \alpha = 0) + S(\rho)\alpha^2, \tag{1.1}$$

where $\alpha = \frac{\rho_n - \rho_p}{\rho_n + \rho_p}$ represents the asymmetry, E_0 represents the symmetric energy per nucleon and S represents the symmetry energy. Thus, understanding the neutron distributions will better constrain the EOS. The EOS is also the bridge that connects nuclear physics and astrophysics; particularly to measure properties of neutron stars.

1.2.2 Astrophysics

From the nuclear physics, more in depth knowledge of the neutron density distributions allows for a more precise measurement of the neutron skin—the difference of the radius of the neutron and proton distribution. The symmetry energy described in the previous section can be expanded about the saturation density of nuclear matter, $\rho_0 \approx 0.16 fm^{-3}$,

$$S(\rho) = S_0 + \frac{L}{3}\left(\frac{\rho - \rho_0}{\rho_0}\right) + \frac{K}{18}\left(\frac{\rho - \rho_0}{\rho_0}\right)^2 + \cdots, \tag{1.2}$$

where L and K represent the first and second derivative of the symmetry energy at saturation density given in Ref [20]. It has been shown that L in particular is highly correlated to the neutron radius of neutron rich nuclei [17, 20, 21]. A precision measurement of the radius of the neutron distribution using CEνNS will allow for the accurate calculation of L and a constraint on the EOS of nuclear matter. Understanding the EOS of nuclear matter will then lead to precise understanding of neutron star properties and structure [22, 23].

Comprehension of the CEνNS cross section and possible deviations from the SM predictions would also play a pivotal role in the explosion mechanism of core-collapse supernova through neutrino-driven convection [24]. CEνNS will also play an important role in the detection of supernova neutrinos with future generations of detectors [25].

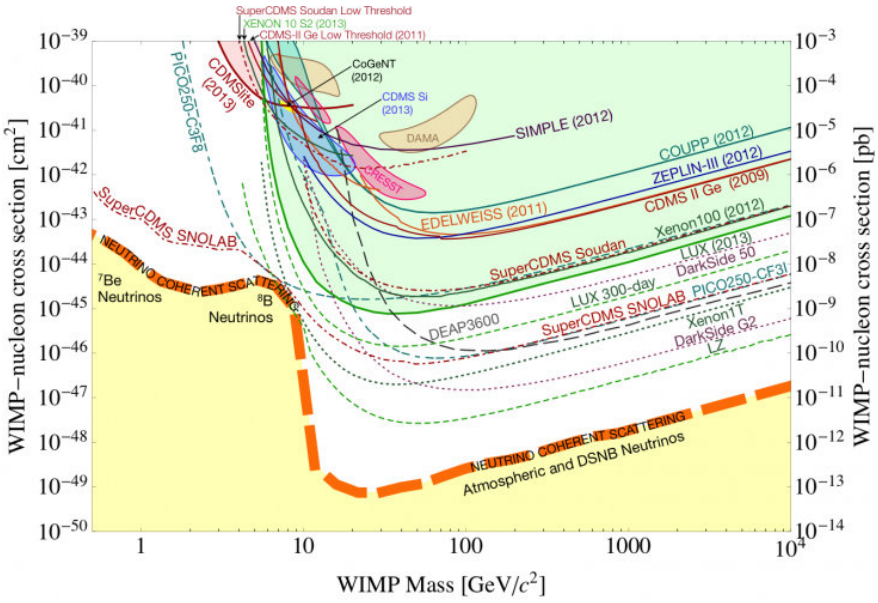

Figure 1.2: The so called 'neutrino floor' (thick, orange line) signifying the limits for dark matter detection. The excluded regions from experiments are represented by the shaded areas and sensitivity of past and future experiments for dark matter searches of WIMPs are represented by the assorted dashed lines. Figure from [2]

1.2.3 Particle Physics

The SM in particle physics has become one of the most robust and successful theories today; however, it is still not enough to fully explain many physical phenomenon. Understanding the CEνNS cross section will be an opportunity to further test the SM and to gain enormous insight into the properties of neutrinos and becomes necessary for the search for dark matter.

If the CEνNS cross sections are precisely comprehended and measured there will be opportunity to test the standard model with an independent measurement of the weak mixing angle, θ_W. For the first time a sensitivity study of the weak mixing angle using CEνNS has been done [26]. The SM is so well constrained at this time any deviations from predictions can be an opportunity for new physics.

Important neutrino properties such as the existence of sterile neutrinos, neutrino magnetic moment, and non-standard interactions (NSI) can also be probed with CEνNS. Investigations into sterile neutrinos has been motivated by recent evidence of an unexpected

excess of the neutrino event rate at MiniBoone [27] and other facilities. A full review of the neutrino properties aforementioned and their relevance to CEνNS has been published concluding that next generation precise measurements of CEνNS will be able to identify and further constrain the SM and NSI model parameters [26].

The CEνNS reactions will also become an important tool for measuring dark matter because it becomes an irreducible background for dark matter detection. The backgrounds for direct detection of Weakly Interacting Massive Particles (WIMPs) becomes increasingly important as sensitivity increases [28]. Figure 1.2 shows the WIMPs discovery limits. If sensitivities for the search of dark matter go below the thick, orange dashed line the CEνNS and WIMP cross sections will be indistinguishable.

CHAPTER 2

FORMALISM

2.1 Coherent Elastic Neutrino Nucleus Scattering Cross Section

In this section, the CEνNS cross section for spinless nuclei will be derived. The cross section is derived in a model-independent formalism using current conservation and Lorentz invariance.

2.1.1 Important Relations

The two-body (i.e., $A+B \rightarrow C+D$), Lorentz invariant differential cross section from [29] is first introduced:

$$\frac{d\sigma}{dt} = \frac{1}{64\pi} \frac{1}{(p_1 \cdot p_2)^2 - m_1^2 m_2^2} \langle |\mathcal{M}|^2 \rangle, \tag{2.1}$$

where $\langle |\mathcal{M}|^2 \rangle$ represents the squared amplitude averaged over initial spins and summed over final spins [30], p_1 (m_1) and p_2 (m_2) are the 4-momenta (mass) of the incoming particles, and $t = Q^2$ is the invariant Mandelstam variable representing the momentum transfer squared.

In Section 2.1.2 the amplitude will be derived using Feynman rules. Following Figure 2.1 the matrix elements and thus the polarized amplitude may be constructed. The vertex factor for the weak neutral interaction is

$$\frac{-ig_z}{2}\gamma^\mu(c_V^f - c_A^f\gamma^5) \xrightarrow{neutrino} \frac{-ig_z}{4}\gamma^\mu(1-\gamma^5), \tag{2.2}$$

where g_z is the coupling to the Z-boson and can be written in terms of the conventional weak couplings, g and g', and weak mixing angle, θ_w,

$$g_z = \frac{g}{\cos\theta_w} = \frac{g'}{\sin\theta_w}, \tag{2.3}$$

where g and g' represent the strength of the coupling to the weak isovector bosons, $\mathbf{W}$, and the isosinglet, B, in Glashow's weak theory [30]. The vector and axial coupling to any

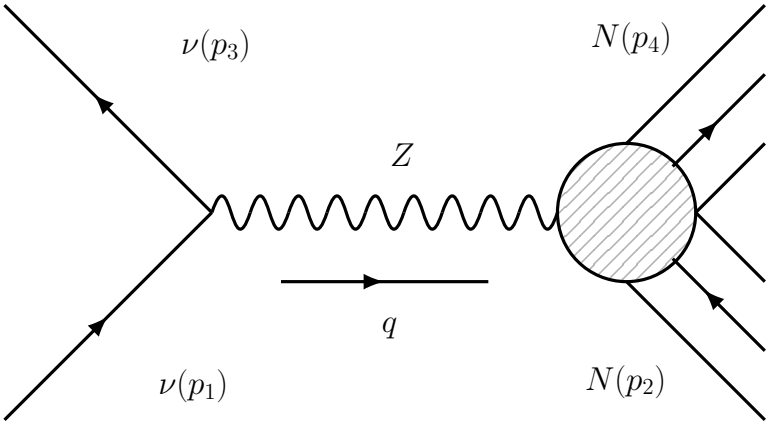

Figure 2.1: The Feynman diagram for CEνNS with p_i and q as the four-momenta and invariant momentum transfer respectively.

fermion, 'f', can be written in terms of its weak isospin, t_3^f, and mixing angle:

$$c_V^f = t_3^f - 2Q_f \sin^2\theta_w, \qquad c_A^f = t_3^f. \tag{2.4}$$

For any flavor of neutrino it follows that $c_A = c_V = \frac{1}{2}$. The spin-1 propagator for the Z-boson in the limit when the propagator mass is much larger than the momentum transfer is written as

$$\frac{-i[g_{\mu\nu} - q_\mu q_\nu / M_z^2]}{q^2 - M_z^2} \xrightarrow{M_z^2 \gg Q^2} \frac{i g_{\mu\nu}}{M_z^2}, \tag{2.5}$$

where $Q^2 = -q^2$ and M_z is the mass of the Z-boson. The mass of the Z-boson can be written in terms of the W-boson mass and mixing angle:

$$M_z = \frac{M_w}{\cos\theta_w}. \tag{2.6}$$

2.1.2 Writing the Amplitude

Now the polarized amplitude is constructed using the above definitions:

$$\begin{aligned} -i\mathcal{M} &= \left[\bar{u}(3)\frac{ig_z}{4}\gamma^\mu(1-\gamma^5)u(1)\right]\left(\frac{-ig_{\mu\nu}}{M_z^2}\right)\left[\frac{ig_z}{4}\langle p_4|\hat{J}_w^\nu|p_2\rangle\right], \\ \mathcal{M} &= -\left(\frac{g_z^2}{16M_z^2}\right)[\bar{u}(3)\gamma^\mu(1-\gamma^5)u(1)][\langle p_4|\hat{J}_\mu^w|p_2\rangle], \end{aligned} \tag{2.7}$$

where $\hat{J}^w_\nu$ is the neutral current operator, and the spinors are labeled with their respective particle momentum for simplicity, (e.g. (1) represents $\nu(p_1)$), using Figure 2.1.

Using (2.7) the unpolarized amplitude squared is written as,

$$\begin{aligned}\langle|\mathcal{M}|^2\rangle &= \left(\frac{g_z^2}{16M_z^2}\right)^2 L^{\mu\nu}H_{\mu\nu} \\ &= \frac{G_F^2}{8}L^{\mu\nu}H_{\mu\nu},\end{aligned} \tag{2.8}$$

where the Fermi coupling constant is introduced:

$$G_F = \frac{1}{4\sqrt{2}}\left(\frac{g}{M_w}\right)^2 = \frac{1}{4\sqrt{2}}\left(\frac{g_z}{M_z}\right)^2, \tag{2.9}$$

where (2.3) and (2.6) have been used to relate the couplings and masses to the conventional quantities, namely, M_w and g. In (2.8) the leptonic tensor and the hadronic tensor are defined as

$$L^{\mu\nu} = |\bar{u}(3)\gamma^\mu(1-\gamma^5)u(1)|^2, \tag{2.10}$$

$$H_{\mu\nu} = |\langle p_4|\hat{J}^w_\mu|p_2\rangle|^2 \tag{2.11}$$

Due to the fact that neutrinos and anti-neutrinos carry only left-handed or right-handed helicity respectively, one does not have to average over initial spins in (2.8).

Derivation of Nucleus Transition Amplitude. Next the general form of the transition amplitude—$\langle p_4|\hat{J}^w_\mu|p_2\rangle$—for the outgoing nucleus is constructed using current conservation and Lorentz invariance. The example from [29] on the pion form factor is followed closely for the following procedure. The current must be a 4-vector, therefore, for the nucleus vertex in Figure 2.1 the only 4-vectors available are p_2, p_4, and q, namely, the incoming and outgoing 4-momentum and the momentum transfer. To conserve momentum the constraint, $p_4 = q + p_2$, is observed and it follows that two independent combinations of available 4-vectors can be constructed as follows,

$$(p_4 + p_2)_\mu\,, \qquad (p_4 - p_2)_\mu = q_\mu. \tag{2.12}$$

It is identified that the only independent scalar at the vertex can be chosen to be q^2 because it can be written in terms of the scalar product of p_4 and p_2. It follows that the 4-vector

combinations can be multiplied by a scalar function without losing its form [29]. In order to model the finite structure of the nucleus the form factor in (2.13) is introduced as the scalar function; it must be a function of the independent variable. The most general form for the weak transition current may now be written, namely,

$$\langle p_4|\hat{J}^w_\mu|p_2\rangle = F(Q^2)\,(p_4+p_2)_\mu + G(Q^2)q_\mu, \tag{2.13}$$

where $F(Q^2)$ and $G(Q^2)$ are the form factor as discussed. Once current conservation is imposed in momentum space (i.e., $q_\mu j^\mu_w = 0$), as required, the second term in (2.13) must vanish, i.e., $G(Q^2) = 0$. With these results the most general form for the neutral current can be written as

$$\langle p_4|\hat{J}^w_\mu|p_2\rangle = Q_w F_w(Q^2)\,(p_4+p_2)_\mu\,, \tag{2.14}$$

with $-q^2 = Q^2$. The form factor has been normalized to $F_w(Q^2=0) = 1$ using Q_w. The weak charge is defined as,

$$Q_w = -N + Z(1 - 4\sin^2\theta_w), \tag{2.15}$$

where N is the neutron number, Z is the proton number, and θ_w is the weak mixing angle with, $\sin^2\theta_w = 0.231$. It follows that because $\sin^2\theta_w \approx \frac{1}{4}$, the second term of the weak charge, Q_w, in (2.15) will be very small, and the $\sim N^2$ enhancement discussed in Chapter 1 will become evident in Subsection 2.1.4.

2.1.3 Evaluating the Amplitude

Casimir's Trick from [30] is now introduced to evaluate the matrix elements:

$$\sum_{all\ \ spins} [\bar{u}(a)\Gamma_1 u(b)][\bar{u}(a)\Gamma_1 u(b)]^* = \mathrm{Tr}[\Gamma_1(\not{p}_b + m_b)\bar{\Gamma}_2(\not{p}_a + m_a)], \tag{2.16}$$

where for this calculation it follows that

$$\Gamma_1 = \gamma^\mu(1-\gamma^5), \qquad \bar{\Gamma}_2 = \gamma^0[\gamma^\nu(1-\gamma^5)]^\dagger\gamma^0 = \gamma^\nu(1-\gamma^5). \tag{2.17}$$

Now using (2.16)—ignoring the neutrino mass—and (2.17), the leptonic tensor can be reduced into a single trace of the form

$$L^{\mu\nu} = \mathrm{Tr}[\gamma^\mu(1-\gamma^5)\not{p}_1\gamma^\nu(1-\gamma^5)\not{p}_3]. \tag{2.18}$$

Evaluating the trace, (2.18), yields

$$\begin{aligned} L^{\mu\nu} &= \mathrm{Tr}[\gamma^{\mu}(1-\gamma^{5})\gamma^{\sigma}p_{\sigma}^{(1)}\gamma^{\nu}(1-\gamma^{5})\gamma^{\lambda}p_{\lambda}^{(3)}] \\ &= 2p_{\sigma}^{(1)}p_{\lambda}^{(3)}\{\mathrm{Tr}[\gamma^{\mu}\gamma^{\sigma}\gamma^{\nu}\gamma^{\lambda}] + \mathrm{Tr}[\gamma^{5}\gamma^{\mu}\gamma^{\sigma}\gamma^{\nu}\gamma^{\lambda}]\} \\ &= 2p_{\sigma}^{(1)}p_{\lambda}^{(3)}\{4(g^{\mu\sigma}g^{\nu\lambda} - g^{\mu\nu}g^{\sigma\lambda} + g^{\mu\lambda}g^{\sigma\nu}) + 4i\epsilon^{\mu\sigma\nu\lambda}\} \\ &= 8\left(p_{1}^{\mu}p_{3}^{\nu} - (p_{1}\cdot p_{3})g^{\mu\nu} + p_{1}^{\nu}p_{3}^{\mu} + ip_{\sigma}^{(1)}p_{\lambda}^{(3)}\epsilon^{\mu\sigma\nu\lambda}\right). \end{aligned} \tag{2.19}$$

In turn, the hadronic tensor can be rewritten using (2.14),

$$\begin{aligned} H_{\mu\nu} &= Q_{w}^{2}F_{w}^{2}[(p_{4}+p_{2})_{\mu}(p_{4}+p_{2})_{\nu}] \\ &= Q_{w}^{2}F_{w}^{2}[4p_{\mu}^{(2)}p_{\nu}^{(2)} + 2p_{\mu}^{(2)}q_{\nu} + 2q_{\mu}p_{\nu}^{(2)} + q_{\mu}q_{\nu}], \end{aligned} \tag{2.20}$$

where the substitution $p_4 = q + p_2$ was made in order to further simplify the calculation by imposing conservation of leptopnic current,

$$q_{\mu}L^{\mu\nu} = L^{\mu\nu}q_{\nu} = 0. \tag{2.21}$$

To adhere to the conservation of the leptonic current any term in (2.20) that contains q_μ will be zero when contracted with the leptonic tensor. Therefore, the hadronic effective tensor can be rewritten without loss of generality as:

$$H_{\mu\nu}^{eff} = 4Q_{w}^{2}F_{w}^{2}(Q^{2})p_{\mu}^{(2)}p_{\nu}^{(2)}. \tag{2.22}$$

Now contracting the leptonic tensor (2.19) with the momentum terms of the effective hadronic tensor in (2.22) yields:

$$\begin{aligned} L^{\mu\nu}p_{\mu}^{(2)}p_{\nu}^{(2)} &= 8(2p_{1}^{\mu}p_{3}^{\nu} - (p_{1}\cdot p_{3})g^{\mu\nu})p_{\mu}^{(2)}p_{\nu}^{(2)} \\ &= 16(p_{1}\cdot p_{2})(p_{3}\cdot p_{2}) - 8(p_{1}\cdot p_{3})p_{2}^{2} \\ &= 16\left[(p_{1}\cdot p_{2})(p_{3}\cdot p_{2}) + \frac{q^{2}p_{2}^{2}}{4}\right], \end{aligned} \tag{2.23}$$

where the Levi-Civita term in (2.19) is omitted because it is anti-symmetric and will cancel after contraction and the dot product in the second term has been replaced for simplicity, i.e., $q^2 = (p_3 - p_1)^2 = -2p_3 \cdot p_1$.

Evaluation in the Lab Frame. Now let's evaluate each term in (2.23) in the lab frame with the nucleus initially at rest. That is,

$$p_1 \cdot p_2 = E_1 M, \tag{2.24}$$

$$\begin{aligned} p_3 \cdot p_2 &= (p_1 + p_2 - p_4)p_2 = p_1 \cdot p_2 + p_2^2 - p_4 \cdot p_2 \\ &= E_1 M + M^2 - E_4 M = M(E_1 + M - E_4) \\ &= M(E_1 - T), \end{aligned} \tag{2.25}$$

$$\begin{aligned} q^2 &= (p_4 - p_2)^2 \\ &= 2M^2 - 2(p_4 \cdot p_2) = 2M^2 - 2ME_4 \\ &= -2MT, \end{aligned} \tag{2.26}$$

where M is the mass of the nucleus, E_1 is the incoming neutrino energy, and $T = E_4 - M$ is the kinetic energy of the recoiling nucleus. To clarify momentum conservation has been used in (2.25) to replace p_3 and pay particular attention to (2.26).

Evaluation of (2.23) in the lab frame using (2.24), (2.26), (2.25) yields,

$$L^{\mu\nu} p_\mu^{(2)} p_\nu^{(2)} = 8M^2 \left[2E(E-T) - MT\right], \tag{2.27}$$

where the incoming neutrino energy has been rewritten as E for simplicity. In turn, this result can be used with (2.22) to evaluate the unpolarized amplitude:

$$\langle |\mathcal{M}|^2 \rangle = 4G_F^2 M^2 \left[2E(E-T) - MT\right] Q_w^2 F_w^2(Q^2). \tag{2.28}$$

2.1.4 Evaluating the Cross-Section

Plugging in (2.28) into (2.1) gives the invariant cross section for CEνNS:

$$\frac{d\sigma_\nu}{dt}(E,T) = \frac{1}{16\pi}\frac{G_F^2}{E^2}\left[2E(E-T) - MT\right] Q_w^2 F_w^2(Q^2). \tag{2.29}$$

Finally, the cross-section is written in terms of the recoil energy, T, by making the substitution $t = 2MT$ for the differential in (2.29) to get our final result:

$$\frac{d\sigma_\nu}{dT}(E,T) = \frac{G_F^2}{8\pi} M \left[2\left(1 - \frac{T}{E}\right) - \frac{MT}{E^2}\right] Q_w^2 F_w^2(Q^2). \tag{2.30}$$

From (2.30) it can be seen that the weak form factor is needed to make predictions on the cross section. The calculation of the form factor is model-dependent and will be discussed in the following section. The total cross section is

$$\sigma_\nu(E) = \frac{G_F^2}{8\pi} M Q_w^2 \int_0^{T_{max}} \left[2\left(1 - \frac{T}{E}\right) - \frac{MT}{E^2} \right] F_w^2(2MT) dT, \tag{2.31}$$

with the maximum recoil energy written as,

$$T_{max} = \frac{2E^2}{2E + M}, \tag{2.32}$$

and where the lower bound of the integral in (2.31) realistically would be the minimum recoil energy that can be detected by the experiment.

2.2 The Form Factor

The form factor encodes the spatial properties and thus the internal structure of the target off which the probe scatters. In the following discussion, the nuclear form factor and the single nucleon form factor will be discussed. The nuclear form factor describing the nucleon distributions will be calculated taking the nucleons as point particles. This is followed by the construction of the charge and weak form factor in which the single-nucleon form factors are folded with the point-nuclear form factors.

2.2.1 Single-Nucleon Form Factor

The single nucleon form factor can be constructed from the charge (electromagnetic) and weak (neutral) currents and will be discussed briefly in this section. The most general and covariant form of the vector part of the single-nucleon charge and weak current can be written from [31] as:

$$\hat{J}^\mu_{EM} = F_1(Q^2)\gamma^\mu + iF_2(Q^2)\sigma^{\mu\nu}\frac{q_\nu}{2M_n}, \tag{2.33}$$

$$\hat{J}^\mu_{NC} = \widetilde{F}_1(Q^2)\gamma^\mu + i\widetilde{F}_2(Q^2)\sigma^{\mu\nu}\frac{q_\nu}{2M_n}, \tag{2.34}$$

where F_1 ($\tilde{F}_1$) and F_2 ($\tilde{F}_2$) are the Dirac and Pauli charge (weak) form factors respectively, and M_n is the nucleon mass. It is more useful to introduce the electric and magnetic Sachs

form factors for scattering; written as linear combinations of the Dirac and Pauli form factors, i.e.,

$$G_E(Q^2) = F_1(Q^2) - \tau F_2(Q^2), \tag{2.35}$$

$$G_M(Q^2) = F_1(Q^2) + F_2(Q^2), \tag{2.36}$$

where $\tau = \frac{Q^2}{4M_n^2}$. The Dirac and Pauli form factors are now introduced in terms of the Sachs' form factors,

$$F_1(Q^2) = G_E(Q^2) + \left(\frac{\tau}{1+\tau}\right)(G_M(Q^2) - G_E(Q^2)), \tag{2.37}$$

$$F_2(Q^2) = \frac{G_M(Q^2) - G_E(Q^2)}{1+\tau}. \tag{2.38}$$

Plugging (2.37) and (2.38) into the charge current (2.33) yields the charge current in terms of the Sachs' form factors:

$$\hat{J}^{\mu}_{EM} = G_E(Q^2)\gamma^{\mu} + \left(\frac{G_M(Q^2) - G_E(Q^2)}{1+\tau}\right)\left[\tau\gamma^{\mu} + i\sigma^{\mu\nu}\frac{q_{\nu}}{2M_n}\right] \approx G_E(Q^2)\gamma^{\mu}. \tag{2.39}$$

The analogous weak current is obtained by replacing the single-nucleon form factor, $G_E(Q^2) \rightarrow \widetilde{G}_E(Q^2)$. For the ground state of spinless nuclei at small momentum transfer the term in brackets in (2.39) is very small and ignored. Only the electric Sachs nucleon form factor will be used to elucidate the structure of the nucleons for the remainder of the report. Note also that the single-nucleon form factors are assumed to remain the same due to the impulse approximation.

Charge Form Factor. The electric Sachs single-nucleon form factor is obtained from fitting world electron scattering data and reviewed in great detail in Ref [32]. The fits are done using a bounded polynomial z-expansion of the form:

$$G(Q^2) = \sum_{k=0}^{k_{max}} a_k z^k \quad \text{with,} \quad z = \frac{\sqrt{t_c + Q^2} - \sqrt{t_c - t_0}}{\sqrt{t_c + Q^2} + \sqrt{t_c - t_0}}, \tag{2.40}$$

where G represents G_E^p and G_E^n, $t_c = 4m_{\pi}^2$ (m_{π} is the pion mass) and $t_0 = -0.7\ GeV^2$ is chosen as a compromise between the limited Q^2 range for neutron form factors and the broad range for proton cross section data. The global fit parameters can be found in the

Table 2.1: The experimental values used to construct the single-nucleon form factors. The magnetic moment is in Bohr magneton units, the point-nucleon mean square radii has units (fm^2) and the weak vector charge of the proton and neutron have radiative corrections.

μ_p	μ_n	r_p^2	r_n^2	g_v^p	g_v^n
2.793	-1.913	0.772 (fm^2)	-0.116 (fm^2)	0.0712	-0.9877

supplementary material of the reference above. In the supplementary material one will find the proton and neutron data are fit using 12 and 10 global fit parameters respectively. The proton electric form factor is fit to cross section and polarization data. The neutron form factor is fit to the extraction of the individual form factors from experiment. The values used for the mean square radii and the magnetic moments are given in Table 2.1. Note that due to the mean-squared values of the proton and neutron, the neutron form factor is very small compared to the proton form factor.

Electroweak Form Factor. Next, using the underlying quark vector currents from [31],

$$\hat{J}^\mu_{EM} = \sum_{f=1}^{3} Q_f \bar{q}_f \gamma^\mu q_f = \frac{2}{3}\bar{u}\gamma^\mu u - \frac{1}{3}\bar{d}\gamma^\mu d - \frac{1}{3}\bar{s}\gamma^\mu s, \tag{2.41}$$

$$\hat{J}^\mu_{NC} = \sum_{f=1}^{3} g_V^f \bar{q}_f \gamma^\mu q_f = g_V^u \bar{u}\gamma^\mu + g_V^d \bar{d}\gamma^\mu d + g_V^s \bar{s}\gamma^\mu s, \tag{2.42}$$

the single-nucleon charge form factors can be related to the single-nucleon weak form factors. The weak vector charge in (2.42) is related to the weak isospin and mixing angle of the fermion, 'f':

$$g_V^f = 2t_3^f - 4Q_f \sin^2\theta_w. \tag{2.43}$$

The protons and neutrons can be related using the quark vector currents because of isospin symmetry, namely, that the up/down distribution of quarks in the proton is the same as the down/up distribution in the neutron. For simplicity, the strange quark contribution will be omitted because the strange form factor is very small and can be ignored for ground state spinless nuclei in the calculations. With that being said the matrix elements for the neutrons

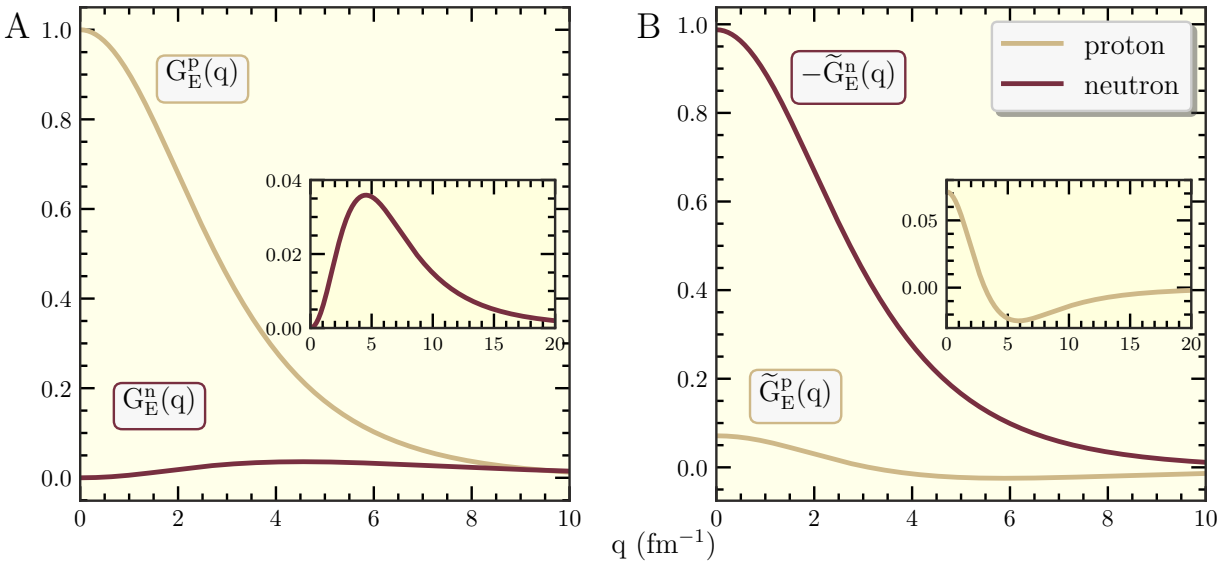

Figure 2.2: (**A**) The single-nucleon electric Sachs form factor for the charge distribution. The inset is meant to show the structure of the neutron charge distribution. (**B**) The single-nucleon electric Sachs form factor for the weak charge distribution. The inset is meant to show the structure of the proton weak distribution.

and protons are constructed using (2.41) for the charged current,

$$\begin{aligned} J^\mu_{EM,p} &= \langle p|\hat{J}^\mu_{EM}|p\rangle = \frac{2}{3}V^\mu_u - \frac{1}{3}V^\mu_d, \\ J^\mu_{EM,n} &= \langle n|\hat{J}^\mu_{EM}|n\rangle = \frac{2}{3}V^\mu_d - \frac{1}{3}V^\mu_u, \end{aligned} \tag{2.44}$$

and (2.42) for the neutral current,

$$\begin{aligned} J^\mu_{NC,p} &= \langle p|\hat{J}^\mu_{NC}|p\rangle = g^u_V V^\mu_u - g^d_V V^\mu_d, \\ J^\mu_{NC,n} &= \langle n|\hat{J}^\mu_{NC}|n\rangle = g^u_V V^\mu_d - g^d_V V^\mu_u, \end{aligned} \tag{2.45}$$

where $V^\mu_{\{u,d\}}$ represents the matrix element of the vector current for the respective quark. Using (2.44) the quark current matrix elements are written in terms of the charge currents. Those are then plugged back into (2.45) to get the neutral currents in terms of the charge currents, i.e.,

$$\begin{aligned} J^\mu_{NC,p} &= g^p_V J^\mu_{EM,p} + g^n_V J^\mu_{EM,n}, \\ J^\mu_{NC,n} &= g^n_V J^\mu_{EM,p} + g^p_V J^\mu_{EM,n}, \end{aligned} \tag{2.46}$$

where the values of g^p_V and g^n_V are given in Table 2.1 and are defined as,

$$g^p_V = 2g^u_V + g^d_V, \qquad g^n_V = g^u_V + 2g^d_V. \tag{2.47}$$

Finally, (2.46) is rewritten in terms of the single-nucleon electric Sachs form factors using (2.39),

$$\begin{aligned}\widetilde{G}_E^p(Q^2) &= g_V^p G_E^p(Q^2) + g_V^n G_E^n(Q^2),\\ \widetilde{G}_E^n(Q^2) &= g_V^n G_E^p(Q^2) + g_V^p G_E^n(Q^2).\end{aligned} \tag{2.48}$$

Note that due to the strength of the weak vector proton charge, g_V^p, and the neutron electric form factor, G_E^n, discussed in the previous section the weak proton Sachs form factor, $\widetilde{G}_E^p(Q^2)$, is much smaller than the weak neutron Sachs form factor, $\widetilde{G}_E^n(Q^2)$. The charge and weak single-nucleon electric Sachs form factors are represented in Figure 2.2 on page 16.

2.2.2 Nuclear Form Factors

The nuclear form factor for point-like nucleons are defined as the Fourier Transform (FT) of the given nucleon density. For example, the point-neutron form factor is written as:

$$F_n(Q^2) = \frac{1}{N}\int d^3\mathbf{r}\; e^{-i\mathbf{Q}\cdot\mathbf{r}}\rho_n(\mathbf{r}), \tag{2.49}$$

where N is the number of neutrons (used as a normalization $F(Q^2 = 0) = 1$) and $\mathbf{Q}$ is a three vector pointing in the direction of momentum transfer with length $Q = \sqrt{\mathbf{q}^2}$. Taking $N \to Z$, where Z is the number of protons, and replacing $\rho_n \to \rho_p$ in (2.49) will give the point-proton form factor. The point-nucleon form factor, (2.49), can be simplified assuming a spherically symmetric object by integrating over the angular dependencies, namely,

$$F_n(Q^2) = \frac{1}{N}\int r^2 dr \left[\frac{4\pi \sin Qr}{Qr}\right]\rho_n(r). \tag{2.50}$$

The nucleon density is defined in terms of the occupied single particle states,

$$\rho_{n,p}(r) = \sum_{\kappa}^{occ}\left(\frac{2j_\kappa + 1}{4\pi r^2}\right)[g^2_{\kappa,\{n,p\}}(r) + f^2_{\kappa,\{n,p\}}(r)], \tag{2.51}$$

where $g(r)$ and $f(r)$ are the upper and lower component of the Dirac spinor and κ is the generalized angular momentum quantum number; these will be discussed further in the next section.

The charge and weak form factors of the nucleus are constructed by folding the single-nucleon form factors with the neutron and proton point-nuclear form factors,

$$\begin{aligned}F_{ch}(Q^2) &= F_n(Q^2)G_E^n(Q^2) + F_p(Q^2)G_E^p(Q^2) \approx F_p(Q^2)G_E^p(Q^2),\\ F_w(Q^2) &= F_n(Q^2)\widetilde{G}_E^n(Q^2) + F_p(Q^2)\widetilde{G}_E^p(Q^2) \approx F_n(Q^2)\widetilde{G}_E^n(Q^2),\end{aligned} \tag{2.52}$$

to introduce the finite structure of the nucleons. In (2.52) G_E ($\widetilde{G}_E$) is the charge (weak) single-nucleon form factor. Note that the charge form factor is dominated by the proton distributions because the neutron distribution is extremely suppressed by the neutron electric form factor, G_E^n. As opposed to the weak form factor that is dominated by the neutron distributions because the proton distribution is extremely suppressed by the proton weak form factor, $\widetilde{G}_E^p$. The single nucleon electric Sachs form factors are graphically represented in Figure 2.2. It can be seen that studying the weak scattering process is needed to better fulfill our understanding of the neutron distributions. For the purposes of this report the exact formulation of (2.52) is used.

Conversely, the density distribution is the Inverse Fourier Transform (IFT) of the form factor. For example, the weak density for a spherical nucleus is

$$\rho_w(\mathbf{r}) = \frac{1}{2\pi^2}\int dQ \left[\frac{\sin Qr}{Qr}\right] Q^2 F_w(Q^2). \tag{2.53}$$

The density distributions are more intuitive than the form factors because they describe the structure in coordinate space. For example, the weak density will reveal the weak charge structure with in the nucleus. The charge density, $\rho_{ch}(r)$ follows by replacing the form factor in (2.53) by $F_w(Q^2) \to F_{ch}(Q^2)$.

Form Factor Expansion. As discussed briefly in Subsection 1.2.1, it has been stated that CEνNS provides a model-independent method for extracting the weak radius and neutron radius. It can be done by Taylor expanding the form factor (2.50) about small values of Q^2. The weak form factor is then expanded about small momentum transfer because it is directly measured in the experiments, namely,

$$\begin{aligned} F_w(Q^2) &= \frac{4\pi}{Q_w}\int_0^\infty r^2 dr \left[\left(1 - \frac{Q^2}{6}r^2 + \frac{Q^4}{120}r^4 - \cdots\right)\right]\rho_w(r) \\ &= 1 - \frac{Q^2}{6}\langle R_w^2\rangle + \frac{Q^4}{120}\langle R_w^4\rangle - \cdots, \end{aligned} \tag{2.54}$$

where the expansion is written in terms of the even moments of the density distribution

$$\langle R_n^{2n}\rangle = \frac{4\pi}{Q_w}\int_0^\infty r^{2n+2}\rho_w(r)dr \quad \text{for} \quad n = 0, 1, 2, \ldots, \tag{2.55}$$

and the normalization, in this case the weak charge, is

$$Q_w = 4\pi \int_0^\infty r^2 \rho_w(r) dr. \tag{2.56}$$

The form factor has been normalized to $F(Q^2 = 0) = 1$ by convention. The even moments can be extracted by fitting the experimental form factor data to the form factor expansion (2.54). At small Q^2 values the form factor is dominated by the mean-square radius of the density distribution. The model dependence of the cross section derived in Subsection 2.1.4 is entirely in the form factor, for which it can be categorized by the mean-squared radius. Note that this expansion formalism remains the same for the charge form factor and the point-nuclear form factors with appropriate normalization using (2.56).

2.3 Mean Field Approximation

A class of relativistic mean field approximations are used to model the behavior of the neutrons and protons within the nucleus. The mean field approach allows one to model the complex many-body problem using the individual nucleon bound states. In the following discussion, the relativistic mean field approach is shown in order to calculate the point-nucleon densities, and in turn the nuclear form factors.

2.3.1 Effective Lagrangian

In order to model the complex interactions of the nucleus in its ground state an effective Lagrangian, that has been extensively researched and refined in the literature, is introduced [33, 34, 35]

$$\begin{aligned}\mathcal{L}_{eff} = &\bar{\psi}\left[\gamma^\mu\left(i\partial_\mu - g_v V_\mu - \frac{g_\rho}{2}\boldsymbol{\tau}\cdot\mathbf{b}_\mu - \frac{e}{2}(1+\tau_3)A_\mu\right) - (M - g_s\phi)\right]\psi \\ &+ \frac{1}{2}\left(\partial^\mu\phi\partial_\mu\phi - m_s^2\phi^2 - \frac{1}{2}V^{\mu\nu}V_{\mu\nu} + m_v^2 V^\mu V_\mu - \frac{1}{2}\mathbf{b}^{\mu\nu}\cdot\mathbf{b}_{\mu\nu} + m_\rho^2\mathbf{b}^\mu\cdot\mathbf{b}_\mu - \frac{1}{2}F^{\mu\nu}F_{\mu\nu}\right) \\ &- \frac{\kappa}{3!}(g_s\phi)^3 + \frac{\lambda}{4!}(g_v V_\mu)^4 - \frac{\zeta}{4!}g_v^4(V_\mu V^\mu)^2 - [\Lambda_s(g_s\phi)^2 + \Lambda_v(g_v^2 V_\mu V^\mu)](g_\rho^2\mathbf{b}_\mu\cdot\mathbf{b}^\mu),\end{aligned} \tag{2.57}$$

where ψ represents the isodoublet nucleon field, A^μ is the photon field, ϕ is the isoscalar scalar field for the σ-meson, V^μ is the isoscalar vector field for the ω-meson, and $\mathbf{b}^\mu$ is the isovector

vector field for the ρ-meson. The isoscalar mesons can not differentiate the nucleons with in the nucleus; conversely, the isovector mesons are able to differentiate the nucleons. The first, second and third lines in (2.57) represent the Yukawa couplings between the nucleons and mesons, the field equations for the massive mesons and photons, and non-linear self and mixed meson interactions respectively. The third line of the effective Lagrangian is used to model the complex many-body interactions with a few parameters that are fit to the bulk properties of nuclei. The parameters κ and λ control the non-linear scalar interactions, ζ controls the quartic vector self-interaction, and Λ_v controls the mixed isoscalar-isovector interaction; for our calculation $\Lambda_s = 0$. Solving the Euler-Lagrange equations of motions leads to the Klein-Gordon equation for the meson sources and the Dirac equation for the particles. The potentials are then provided from a self-consistent calculation described in Ref [33] and references therein. These models form a class that predict very well the known properties of nuclear matter and only differ in the choice of parameters.

For this report it was useful to rewrite the fields described in (2.57) into its single-nucleon scalar and vector potentials for the spherically symmetric system

$$\begin{aligned} S_p(r) = S_n(r) = -g_s\phi(r), \quad V_p(r) &= g_v V(r) + \frac{g_\rho b(r)}{2} + A(r), \\ V_n(r) &= g_v V(r) - \frac{g_\rho b(r)}{2}, \end{aligned} \tag{2.58}$$

where $\phi(r)$, $V(r)$, $b(r)$ and $A(r)$ are the fields in the ground state mean-field limit [33]. These single-nucleon potentials will be used in the following section to calculate the single-nucleon occupied energy levels and wave functions.

2.3.2 Dirac Equation

First, the Dirac equation for the single nucleon vector and scalar potentials of the protons and neutrons are evaluated individually by solving the eigenvalues for the Hamiltonian:

$$\left(\boldsymbol{\alpha}\cdot\mathbf{p} + \beta[m + S(r)]\right)\Psi(\mathbf{x}) = \left[E - V_{\{n,p\}}(r)\right]\Psi(\mathbf{x}) \tag{2.59}$$

where m is the nucleon mass, $\Psi(\mathbf{x})$ is the 4-component Dirac spinor, and E is the Dirac energy subject to $E < m$ for bound-state solutions. The scalar and vector potentials transform like

a Lorentz scalar and time-component of a four-vector respectively, and $\boldsymbol{\alpha}$ and β are matrices defined as,

$$\boldsymbol{\alpha} = \begin{pmatrix} 0 & \boldsymbol{\sigma} \\ \boldsymbol{\sigma} & 0 \end{pmatrix}, \quad \beta = \begin{pmatrix} \mathbb{I} & 0 \\ 0 & -\mathbb{I} \end{pmatrix}, \tag{2.60}$$

where $\boldsymbol{\sigma}$ represents the Pauli matrix and $\mathbb{I}$ represents the identity matrix. The radial single-particle solutions to (2.59) can be written in the form:

$$\Psi_{n\kappa m}(\mathbf{x}) = \begin{bmatrix} \psi_a \\ \psi_b \end{bmatrix} = \frac{1}{r} \begin{bmatrix} g_{n\kappa}(r)\mathcal{Y}_{\kappa m}(\hat{\mathbf{x}}) \\ i f_{n\kappa}(r)\mathcal{Y}_{-\kappa m}(\hat{\mathbf{x}}) \end{bmatrix}, \tag{2.61}$$

where n and m are the principal and magnetic quantum numbers respectively, $\hat{\mathbf{x}}$ is the coordinate operator, and

$$\mathcal{Y}_{\kappa m}(\hat{\mathbf{x}}) = \left\langle \hat{\mathbf{x}} \middle| l\frac{1}{2}jm \right\rangle, \qquad \kappa = \pm\left(j + \frac{1}{2}\right), \qquad l = \begin{cases} \kappa & \text{if } \kappa < 0 \\ -1-\kappa & \text{if } \kappa > 0 \end{cases}, \tag{2.62}$$

are the spin-angular functions, generalized angular momentum, κ, and the cases for the orbital angular momentum, l, respectively. Note that the 4-component Dirac spinor, Ψ, does not conserve orbital angular momentum, whereas, the upper and lower component wave functions (ψ) do. Furthermore, the subtle description determines spin orbit partners where the single particle wave function has the same l-value but different κ-values described by (2.62). In (2.61) the phase convention, multiplying the lower component by imaginary i, assures that $g(r)$ and $f(r)$ are real bound-state wave functions and the spin-angular functions are used because $\Psi(\hat{\mathbf{x}})$ has definite parity [36]. The normalization condition is as follows,

$$\int_0^\infty dr\ [g_{n\kappa}^2(r) + f_{n\kappa}^2(r)] = 1. \tag{2.63}$$

Now (2.59) can be rewritten using (2.61), i.e.,

$$\begin{pmatrix} m + S(r) & \boldsymbol{\sigma}\cdot\mathbf{p} \\ \boldsymbol{\sigma}\cdot\mathbf{p} & -m - S(r) \end{pmatrix} \begin{bmatrix} \psi_a \\ \psi_b \end{bmatrix} = \begin{pmatrix} E - V(r) & 0 \\ 0 & E - V(r) \end{pmatrix} \begin{bmatrix} \psi_a \\ \psi_b \end{bmatrix}, \tag{2.64}$$

and separated into two first order equations:

$$\begin{aligned} [E - V(r) - m - S(r)]\,\psi_a - \boldsymbol{\sigma}\cdot\mathbf{p}\ \psi_b = 0, \\ [E - V(r) + m + S(r)]\,\psi_b - \boldsymbol{\sigma}\cdot\mathbf{p}\ \psi_a = 0. \end{aligned} \tag{2.65}$$

Using the Pauli matrix relations,

$$(\boldsymbol{\sigma}\cdot\mathbf{x})(\boldsymbol{\sigma}\cdot\mathbf{p}) = \mathbf{x}\cdot\mathbf{p} + i\boldsymbol{\sigma}\cdot(\mathbf{x}\times\mathbf{p}), \qquad (\boldsymbol{\sigma}\cdot\mathbf{x})^2 = |\mathbf{x}|^2 = r^2, \tag{2.66}$$

the dot product can be rewritten as:

$$\begin{aligned}\boldsymbol{\sigma}\cdot\mathbf{p} &= \frac{1}{r^2}(\boldsymbol{\sigma}\cdot\mathbf{x})(\boldsymbol{\sigma}\cdot\mathbf{x})(\boldsymbol{\sigma}\cdot\mathbf{p}) \\ &= \frac{1}{r^2}(\boldsymbol{\sigma}\cdot\mathbf{x})\left[\mathbf{x}\cdot\mathbf{p} + i\boldsymbol{\sigma}\cdot(\mathbf{x}\times\mathbf{p})\right] \\ &= (\boldsymbol{\sigma}\cdot\hat{\mathbf{r}})\left[\hat{\mathbf{r}}\cdot\mathbf{p} + i\,\frac{\boldsymbol{\sigma}\cdot\mathbf{L}}{r}\right]. \end{aligned} \tag{2.67}$$

Next, the relations for the operators acting on the two-component wave function are:

$$(\hat{\mathbf{r}}\cdot\mathbf{p})\psi_{a,b} = -i\frac{\partial\psi_{a,b}}{\partial r}, \tag{2.68}$$

$$\begin{aligned}(\boldsymbol{\sigma}\cdot\mathbf{L})\psi_{a,b} &= (\mathbf{J}^2 - \mathbf{S}^2 - \mathbf{L}^2)\psi_{a,b} \\ &= \left(j(j+1) - l(l+1) - \frac{3}{4}\right)\psi_{a,b} \\ &= (\kappa - 1)\psi_{a,b}, \end{aligned} \tag{2.69}$$

and the final operator $(\boldsymbol{\sigma}\cdot\hat{\mathbf{r}})$ acting on the spin-angular function will choose the other available l-value (negative κ-value) and acts like

$$(\boldsymbol{\sigma}\cdot\hat{\mathbf{r}})\mathcal{Y}_{\kappa m} = -\mathcal{Y}_{-\kappa m}. \tag{2.70}$$

Applying (2.68), (2.69) and (2.70) on (2.65) results in two ordinary differential equations used to find the bound-state wave functions, i.e.,

$$\begin{aligned}\left[\frac{d}{dr} + \frac{\kappa}{r}\right] g_{n\kappa}(r) - \left[E - V_{\{n,p\}}(r) + m + S_{\{n,p\}}(r)\right] f_{n\kappa}(r) = 0, \\ \left[\frac{d}{dr} - \frac{\kappa}{r}\right] f_{n\kappa}(r) + \left[E - V_{\{n,p\}}(r) - m - S_{\{n,p\}}(r)\right] g_{n\kappa}(r) = 0. \end{aligned} \tag{2.71}$$

The wave functions of the coupled ordinary differential equations (2.71) are solved for the protons and neutrons numerically using a forth-order Runge-Kutta method with boundary conditions.

CHAPTER 3

RESULTS

3.1 Mean Field Results

Several calibrated relativistic mean field models are used to predict the point-nuclear form factors for various nuclei of interest. The noble gases, Argon-40 and Xenon-132 are studied because of their continued interest and applicability for dark matter detectors [37]. Iodine-127 and Cesium-133 are studied because of their use in the recent experimental achievement to measure CEνNS. The formalism provided in this report is particularly geared towards spinless, symmetric nuclei, namely, even number of protons and neutrons. Pairing effects due to the unpaired nucleons and deformation of the nucleus are not accounted for. This is important to mention because Iodine-127 and Cesium-133 have an uneven number of protons. The contributions from the unpaired proton in Iodine-127 and Cesium-133 need to be further studied. Showing the similarities of the density distributions of Xenon to that of Cesium and Iodine in this report gives us some quantitative evidence that the effects due to the unpaired proton are minimal.

Taking the IFT of the nuclear form factor yields the density distribution for point-nucleons as discussed in Subsection 2.2.2. From the density distributions the root-mean-square radii are calculated using (2.55), i.e., $R = \sqrt{\langle r^2 \rangle}$. The predicted values for the root-mean-square radii are shown in Table 3.1 on page 32. The models used in this report have been chosen by analyzing the neutron skin, $R_n - R_p$, of Lead-208. Moreover, the models that gave a wide range of values for the neutron skin were chosen to reflect a wide range of predicted values for the radius of the neutron distribution.

Using the nuclear mean-field potentials (2.58) for the ground state nucleus and solving the coupled first order Dirac equations, (2.71), produced the result for the Dirac spinors, namely, the lower and upper component bound-state wave functions. In addition, the lower and upper wave functions are used the calculate the proton and neutron density distributions

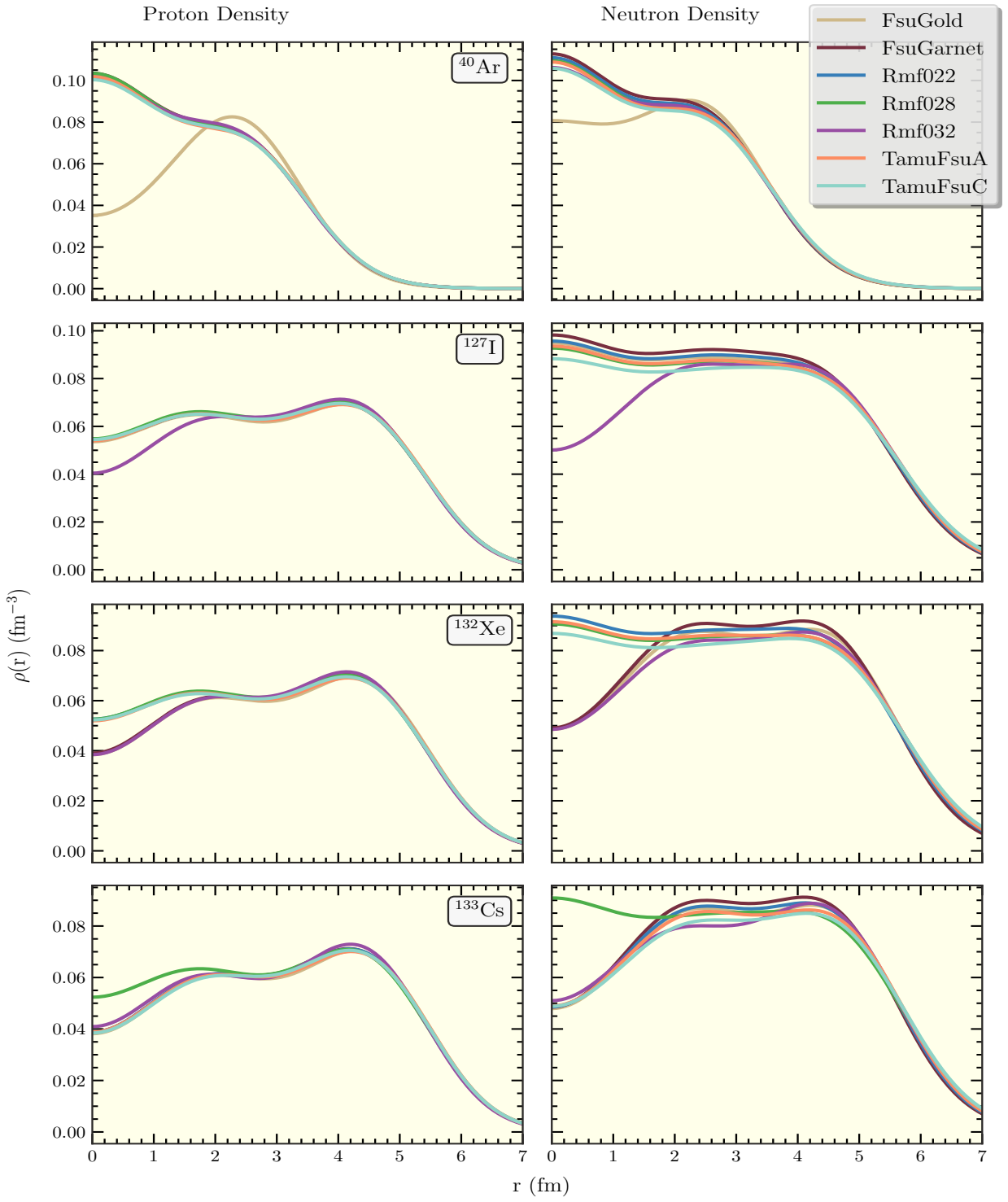

Figure 3.1: Point-nuclear density distributions are calculated using the models listed. Each row shares the y-axes and corresponds to a given nucleus as labeled. The first and second columns share the x-axes and represent the proton and neutron distributions respectively.

using (2.51). Figure 3.1 shows the results of calculating the neutron and proton densities for the four nuclei of interest in this study.

The model predictions for the radius of the proton distributions agree within $\sim 1\%$ with the experimental values; this reflects the fact that our models for the proton distributions are well constrained by experiment. In contrast, one can see that the neutron distributions have much greater deviations depending on the model because it is much less constrained. In other words the isoscalar sector of the interaction is well understood through various hadronic probes as discussed in 1.2.1. On the contrary, the isovector sector of the weak interaction is not well understood; CEνNS will allow the isovector sector parameters to be much better constrained.

The density distributions that tend to have a lower value at the origin, commonly called a 'hole', is due to the model choice of occupied energy levels. The behavior of the wave function at the origin goes like $\sim r^{l+1}$, therefore, is dominated by the $l = 0$ bound-state energy solutions. This is due to the linear behavior at the origin of the wave functions for $l = 0$ states, compared to a slower increase at the origin for higher orbital angular momentum. The subtlety of the 'hole' comes from the fact that the energy levels are almost degenerate with differences in energies on the order of an MeV to keV for the shell closure. For example, FsuGold model predicts a 'hole' for the proton density distribution because the $D_{5/2}$ orbital has a lower energy than the $S_{1/2}$ and thus closes the shell.

The mean-field density predictions are used to calculate the point-nucleon form factors by taking the FT using (2.50). These results will be used to compute the experimentally accessible charge and weak form factors in the next Section.

3.2 Experimentally Accessible Results

The experimentally accessible quantities pertinent to this study come in the form of the charge and weak nuclear form factor and the CEνNS cross section discussed in Section 2.1.

3.2.1 Form Factor

As discussed in the previous section the Fourier transform of the nuclear densities of the point-nucleons of Figure 3.1 can be used to obtain the nuclear form factors. Using (2.52), the nuclear form factors are folded with the single-nucleon electric Sachs form factors of Figure 2.2; Figure 3.2 shows the results of this procedure. The absolute value of the form factor, $|F(q)|$, is taken in order to show the oscillatory behavior on a log plot. This procedure allows for the diffraction minimum of the form factor to be seen. These 'dips' are characteristic minimum values of the form factor at specific momentum transfer due to the oscillations at larger q-values. Note that the minimum q-values increase in frequency and shift to slightly smaller values for larger and more neutron rich nuclei; the first minimum value, q_0, is shown in Figure 3.2 for the heavier elements. At small momentum transfer the form factor is almost model independent. Comparing the weak and charge form factors, it can be seen that momentum transfers where the minima in the form factor occur are slightly smaller. The minima of the form factors occur at slightly smaller momentum transfer for heavier nuclei because the exponential decay of the form factor is dominated by the mean-squared radius of the density distribution.

Figure 3.3 shows that our results using various relativistic mean field models agree fairly well with the parity violating electron scattering experiment done by the PREX collaboration [3]. From the data the form factor was extracted at a value of $\bar{q} = 0.475$ fm^{-1} with a weak radius of $R_w = 5.836(182)$ where the model and experimental errors are added in quadrature. This figure also illuminates the extreme difficulty and sensitivity needed in the experiments to constrain the models. In order to differentiate the theoretical models the error bars need to be reduced to $\sim 0.1\%$ error.

Figure 3.4 shows the charge and weak density obtained from taking the FT of the respective form factor after folding with the single nucleon form factors.

Comparison of the point-nuclear density distributions with the charge and weak density distribution shows almost identical results. This confirms, as it should be, that the charge distribution is almost entirely sensitive to the distribution of protons and the weak distribution are conversely sensitive to the neutrons in the nucleus. This is a result of the charge

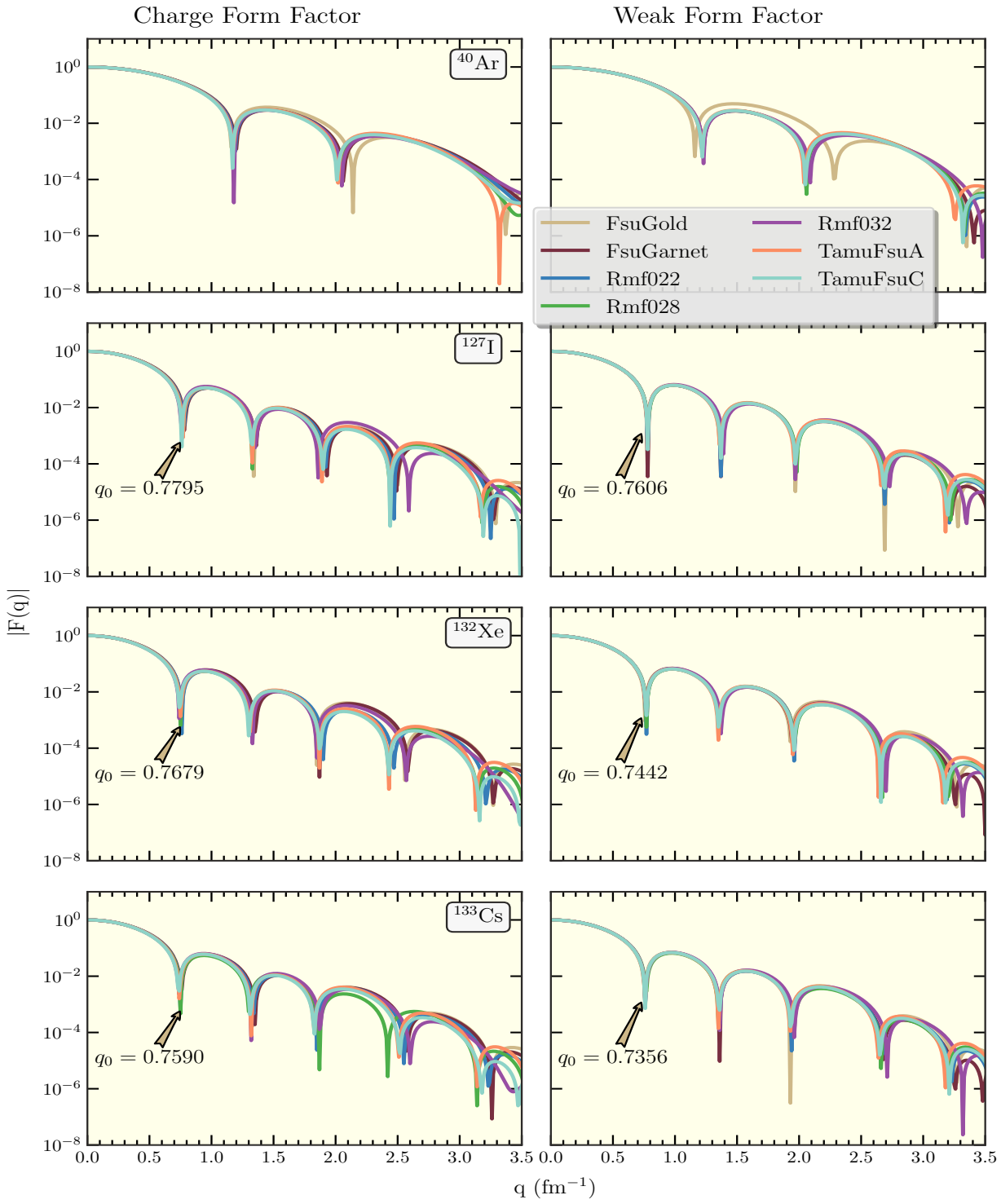

Figure 3.2: Nuclear charge and weak form factors from folding the single-nucleon form factors with the point-nuclear form factors. The columns and rows follow the same procedure as Figure 3.1.

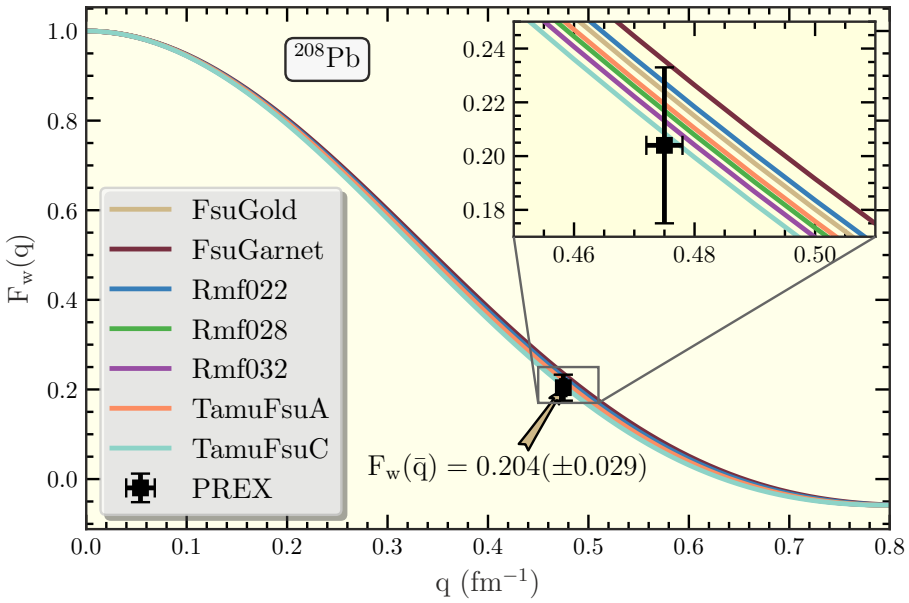

Figure 3.3: The weak form factor of ^{208}Pb for various models and the experimentally extracted weak form factor from parity violating electron scattering experiment, PREX [3]. The inset zooms in on the experimental point to compare our results.

of the protons and the weak charge of the neutrons. The charge of the protons couples very strongly to the electromagnetic interaction, where the neutrons are neutral. Conversely, the neutrons couple very strongly to the weak interaction and the protons have almost no weak charge.

To gain a better understanding of the form factor we can introduce an analytic form of the form factor using the symmetrized Fermi function described in full detail in Ref [38]. The form factor for the spherically symmetric nuclei using the symmetrized Fermi density is given as:

$$F_{sf}(q) = \frac{3\pi a}{qc[c^2+\pi^2a^2]}\left[\frac{1}{\sinh \pi qa}\right]\left[\frac{\pi a}{\tanh \pi qa}\sin qc - c\cos qc\right], \tag{3.1}$$

where a and c are the so called surface diffuseness and half-density radius respectively; better known from the Fermi density $\rho(r) = \frac{\rho_0}{1+e^{(r-c)/a}}$. Taking (3.1) at large momentum transfer yields:

$$F_{sf} \Longrightarrow -\frac{6\pi a}{\sqrt{c^2+\pi^2a^2}}\frac{\cos(qc+\beta)}{qc}e^{-\pi qa}, \quad \text{where} \quad \beta = \tan^{-1}\frac{\pi a}{c}, \tag{3.2}$$

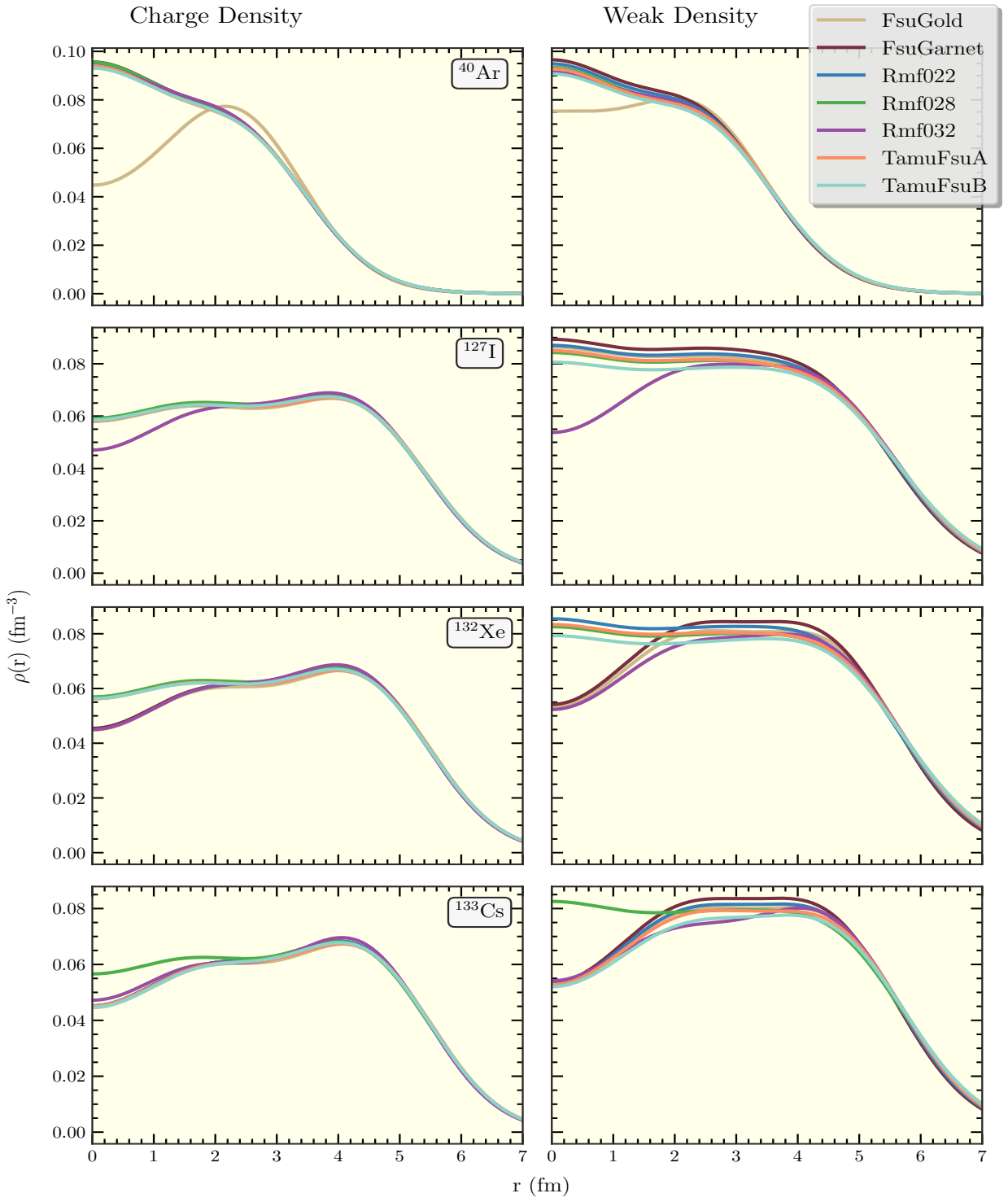

Figure 3.4: Nuclear charge and weak density distributions calculated from the charge and weak form factors for the models shown. The columns and rows follow the same procedure as Figure 3.1.

where asymptotically $\sinh x \to \frac{e^x}{2}$, $\tanh x \to 1$ and the trigonometric identity, $-\cos(\alpha+\beta) = \sin\alpha\sin\beta - \cos\alpha\cos\beta$, have been used. One can see clearly from the asymptotic form of (3.1) that the exponential decay of the form factor is due to the surface diffuseness, a, and the oscillations are controlled by the half-density radius, c.

Qualitative analysis of the density distributions show how the half-density and surface diffuseness affect the form factors. Comparing the density distributions for Argon-40 and the heavier nuclei one can see that the half-density parameter is smaller. For smaller nuclei the form factor has fewer oscillations and they begin at higher descent indicative of a smaller half-density. The surface diffuseness indicates how steep the decent of the density distributions are and translates to the rate of exponential decay in the form factor. From this quantitative analysis it is shown that the heavier nuclei have larger surface diffuseness and half-density distances leading to larger exponential decay and oscillations at smaller q-values.

The weak skin form factor can be constructed by subtracting the charge form factor from the weak form factor distributions, (3.2). Taking the form factor expansion, (2.54), to the first moment gives us an approximate form for the weak skin, namely,

$$\begin{aligned} F_{ch}(Q^2) - F_w(Q^2) &\approx (1 - \frac{Q^2}{6}R_{ch}^2) - (1 - \frac{Q^2}{6}R_w^2) \\ &= \frac{Q^2}{6}(R_w^2 - R_{ch}^2) \\ &= \frac{Q^2}{6}(R_w + R_{ch})(R_w - R_{ch}). \end{aligned} \tag{3.3}$$

In (3.3) the weak skin form factor, $F_{ch} - F_w$, is directly proportional to the weak skin, $R_w - R_{ch}$. This is of great importance for experimental analysis because the weak and charge form factor are what is measured directly. With this formalism the weak skin may be extracted in a model-independent way. The weak skin form factor is shown for the four studied nuclei in Figure 3.5. From Figure 3.5, it can be seen that the curvature near the origin and the peaks of the form factor are controlled by the weak skin. Furthermore, the slope of the weak form factor is larger for the more neutron rich matter and the models with larger weak skin have greater peaks, as they should.

From the density distributions one can extract the root-mean-square radius as discussed earlier. Experimentally the root-mean-square radius is extracted from the first even moment

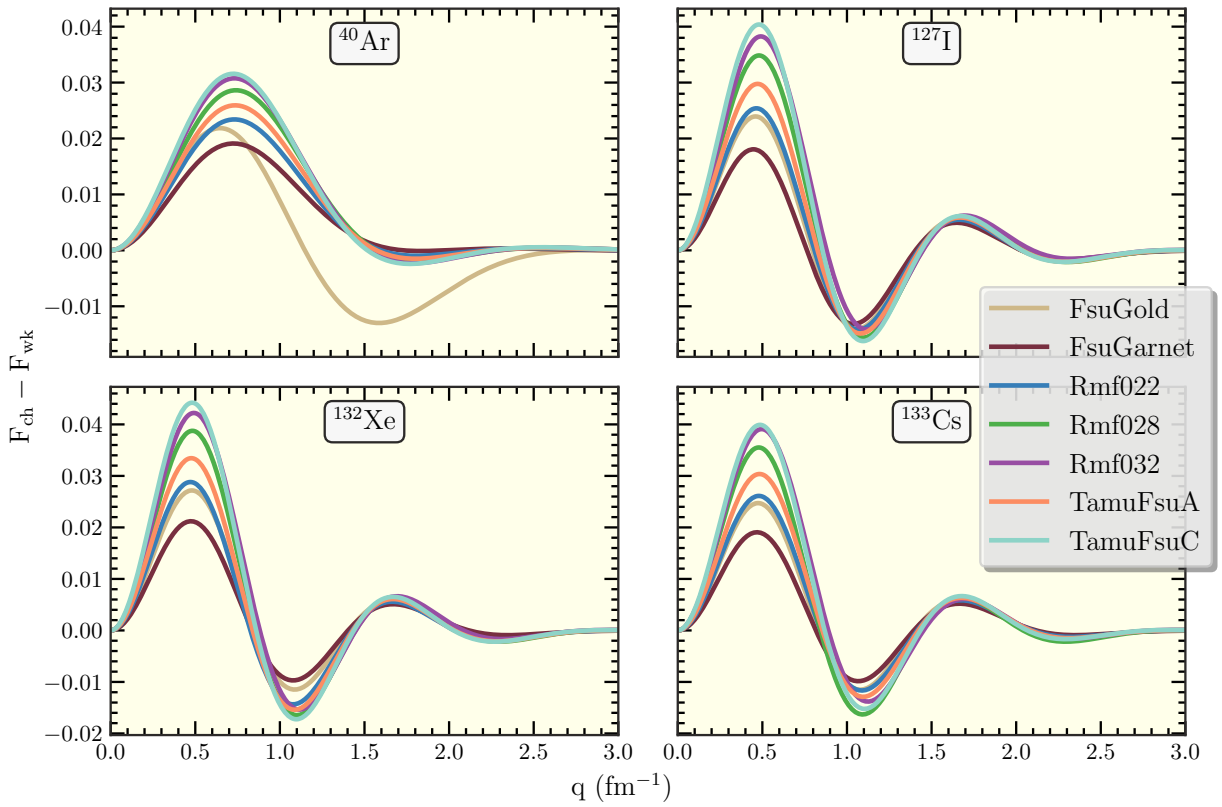

Figure 3.5: The nuclear weak skin form factor, $F_{ch} - F_w$, is shown for all the models used in this report.

of the form factor expansion as discussed in Subsection 2.2.2. Specifically, the charge radius of many nuclei have been extensively researched and are very well known. It is shown that our models agree very well with the experimental charge radii of the nuclei of study by comparing the calculated and experimental values in Table 3.1. Note that for a particular nucleus the proton and charge radii are fairly consistent. In contrast, the neutron distributions are poorly known and the neutron and weak radii vary largely from model to model. One can see the experimental results of the charge root-mean-square radii and some initial experimental values for the neutron and weak radii to compare with our results. The experimental rows of Table 3.1 show charge radius results from a combination of muonic spectra and electron scattering data [9], recent results for Calcium-40 and Calcium-48 of the neutron skin [13] using proton scattering with hadronic model dependent errors, and weak neutron radius of

Lead-208 from parity violating electron scattering [3].

Table 3.1: Theoretically calculated root-mean-squared radii from the seven relativistic mean field models, showing the neutron and proton radii, neutron skins, charge and weak radii, and weak skins extracted from the predicted density distributions.

Nucleus	Model	R_p	R_n	$R_n - R_p$	R_{ch}	R_w	$R_w - R_{ch}$
^{40}Ca	FsuGold	3.337	3.286	-0.0512	3.426	3.372	-0.0538
	FsuGarnet	3.345	3.292	-0.0522	3.433	3.378	-0.0548
	Rmf022	3.351	3.299	-0.0517	3.439	3.385	-0.0543
	Rmf028	3.350	3.300	-0.0495	3.438	3.386	-0.0520
	Rmf032	3.357	3.309	-0.0479	3.445	3.395	-0.0503
	TamuFsuA	3.358	3.307	-0.0501	3.446	3.393	-0.0527
	TamuFsuC	3.374	3.329	-0.0455	3.462	3.414	-0.0478
	Experiment [9, 13]	3.385	3.375	$0.010^{+0.048}_{-0.049}$	3.4776(19)		
^{40}Ar	FsuGold	3.253	3.363	0.1106	3.343	3.459	0.1166
	FsuGarnet	3.269	3.350	0.0807	3.358	3.444	0.0857
	Rmf022	3.270	3.367	0.0970	3.359	3.462	0.1026
	Rmf028	3.266	3.382	0.1156	3.355	3.477	0.1217
	Rmf032	3.266	3.393	0.1269	3.355	3.489	0.1334
	TamuFsuA	3.277	3.383	0.1058	3.366	3.478	0.1116
	TamuFsuC	3.282	3.414	0.1318	3.371	3.510	0.1385
	Experiment [9]				3.4274(29)		
^{48}Ca	FsuGold	3.365	3.562	0.1972	3.451	3.657	0.2063
	FsuGarnet	3.365	3.563	0.1971	3.451	3.658	0.2062
	Rmf022	3.356	3.553	0.1966	3.442	3.648	0.2056
	Rmf028	3.352	3.584	0.2315	3.438	3.680	0.2415
	Rmf032	3.345	3.589	0.2438	3.432	3.686	0.2541
	TamuFsuA	3.366	3.581	0.2144	3.452	3.676	0.2240
	TamuFsuC	3.366	3.616	0.2501	3.452	3.713	0.2606
	Experiment [9, 13]	3.387	3.555	$0.168^{+0.052}_{-0.055}$	3.4771(22)		
^{127}I	FsuGold	4.665	4.830	0.1646	4.727	4.901	0.1739
	FsuGarnet	4.655	4.785	0.1305	4.717	4.856	0.1384
	Rmf022	4.650	4.821	0.1717	4.712	4.893	0.1811
	Rmf028	4.640	4.862	0.2221	4.703	4.936	0.2335
	Rmf032	4.637	4.872	0.2345	4.700	4.946	0.2464
	TamuFsuA	4.660	4.855	0.1952	4.722	4.928	0.2056
	TamuFsuC	4.655	4.913	0.2575	4.718	4.988	0.2703
	Experiment [9]				4.7500(81)		

Table 3.1 - continued

Nucleus	Model	R_p	R_n	$R_n - R_p$	R_{ch}	R_w	$R_w - R_{ch}$
^{132}Xe	FsuGold	4.713	4.885	0.1714	4.775	4.956	0.1809
	FsuGarnet	4.692	4.829	0.1368	4.754	4.899	0.1449
	Rmf022	4.690	4.879	0.1884	4.752	4.951	0.1985
	Rmf028	4.683	4.925	0.2420	4.745	4.999	0.2541
	Rmf032	4.679	4.935	0.2557	4.741	5.009	0.2682
	TamuFsuA	4.703	4.916	0.2136	4.764	4.989	0.2247
	TamuFsuC	4.6991	4.976	0.2776	4.760	5.051	0.2910
	Experiment [9]				4.7859(52)		
^{133}Cs	FsuGold	4.733	4.891	0.1580	4.795	4.962	0.1670
	FsuGarnet	4.713	4.838	0.1251	4.774	4.907	0.1329
	Rmf022	4.712	4.877	0.1646	4.774	4.948	0.1738
	Rmf028	4.705	4.930	0.2243	4.767	5.003	0.2358
	Rmf032	4.695	4.927	0.2322	4.757	5.001	0.2440
	TamuFsuA	4.727	4.915	0.1877	4.789	4.986	0.1979
	TamuFsuC	4.723	4.968	0.2444	4.785	5.042	0.2567
	Experiment [9]				4.8041(46)		
^{208}Pb	FsuGold	5.465	5.669	0.2043	5.518	5.733	0.2150
	FsuGarnet	5.437	5.597	0.1593	5.491	5.659	0.1684
	Rmf022	5.434	5.648	0.2138	5.487	5.712	0.2250
	Rmf028	5.431	5.713	0.2816	5.485	5.780	0.2952
	Rmf032	5.427	5.743	0.3162	5.480	5.811	0.3311
	TamuFsuA	5.449	5.696	0.2470	5.502	5.762	0.2593
	TamuFsuC	5.447	5.774	0.3267	5.500	5.842	0.3420
	Experiment [9, 16]	5.449	5.751	0.302(177)	5.5012(13)	5.826	0.323(183)

3.2.2 Cross Section

The CEνNS cross section can be computed once the weak nuclear form factor is known using (2.31) as discussed in Subsection 2.1.4. Figure 3.6 shows both the differential and total cross section for various nuclei using the FsuGold model. The differential cross section is taken at the energy of a monochromatic neutrino from pion decay at rest. This two-body decay of the form, $\pi^+ \to \mu^+ + \nu_\mu$, produces the monochromatic neutrino energy at 29.9 MeV [1]. Incidentally, the value of the monochromatic neutrino energy from the pion

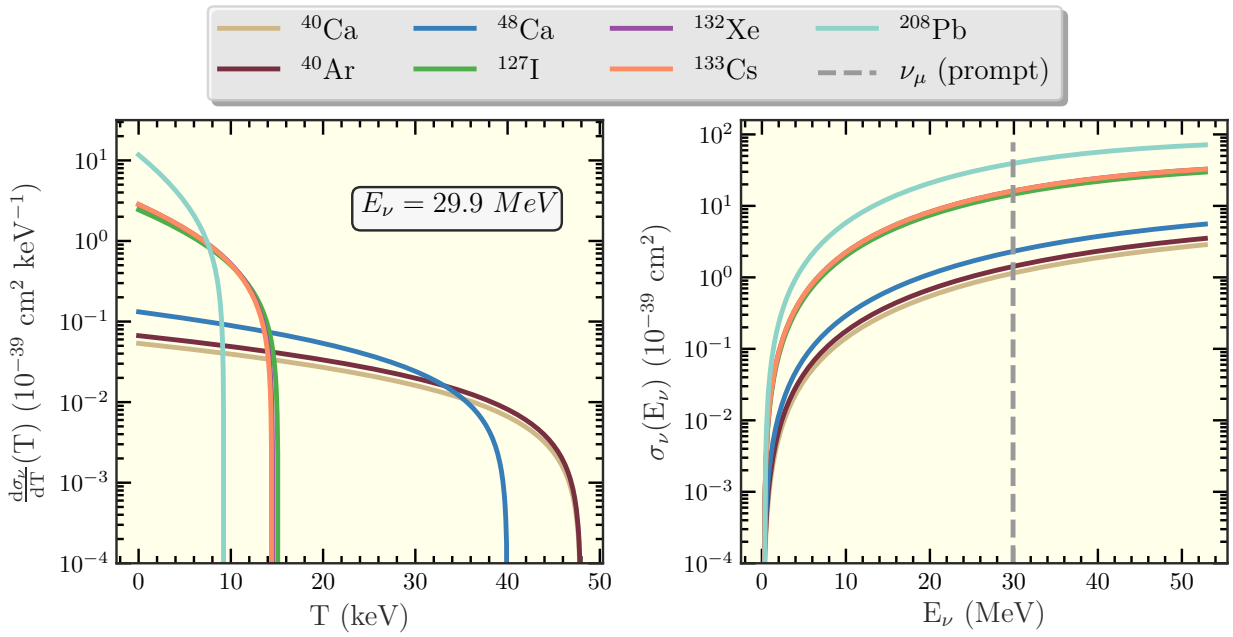

Figure 3.6: (**Left**) The differential cross-section as a function of nuclear recoil energy using the FsuGold Model at incoming neutrino energy of 29.9 MeV. (**Right**) The total cross-section as a function of incoming neutrino energy. The dashed gray line representing the monochromatic neutrino energy for a pion decay at rest.

decay at rest quoted in [1] was a typo; the correct value for the neutrino energy is 29.792 MeV. The maximum nuclear recoil is determined by the mass of the target nuclei and incoming neutrino energy. It is evident that the target material has competing components, namely the number of neutrons and the recoil energy. As discussed in Chapter 1 the enhancement to the differential cross section for larger neutron rich nuclei is offset by the threshold that the nuclear recoil energy can be detected.

The kinematics imposes the maximum recoil energy for the monochromatic neutrino using (2.32) and thus restricts the momentum transfer to $|q|_{max} = 2MT_{max} \sim 0.3\ fm^{-1}$. The recoil energy decreases proportional to the mass of the nucleus leaving $|q|_{max}$ relatively constant for these nuclei. The first even moment of the form factor expansion (2.54) leads to between $15 - 35\%$ correction at maximum momentum transfer. The form factor decays more rapidly for larger nuclei as seen in Figure 3.2. This entails that at the low momentum transfer for CEνNS the larger nuclei have larger corrections due to the form factor. This is

Table 3.2: CEνNS list of cross sections using FSUGold model with and without the form factor corrections as well as the % difference of the two.

$(10^{-39}$ cm$^2)$	^{40}Ca	^{40}Ar	^{48}Ca	^{127}I	^{132}Xe	^{133}Cs	^{208}Pb
σ_ν $(F(0)=1)$	1.284	1.601	2.638	18.439	20.566	20.523	54.030
σ_ν $(F(q))$	1.147	1.421	2.310	14.587	16.182	16.139	39.387
% Diff	11.9	12.6	14.1	26.4	27.0	27.1	37.1

also due to the larger weak skin from the neutron rich nuclei; as discussed earlier the larger skin results in a greater form factor decay and, in turn, larger correction from the form factor. The right portion of Figure 3.6 shows the increasing total cross section as a function of incoming neutrino energy. The dashed gray line again represents the monochromatic neutrino from stopped pion decay. The total cross sections for the monochromatic neutrino energy are represented in Table 3.2. The total cross sections are obtained for the $E_\nu = 29.9$ MeV by integrating the differential cross sections (left) at the gray dashed line (right) of Figure 3.6. It is shown that the form factor gives a correction on the total cross section from $\sim 10 - 40\%$ depending on how neutron rich the target is.

In summary, the results attained from the class of relativistic mean field models has been shown and described in detail. The behavior of the point-nuclear density distributions have been calculated and used to predict the charge and weak form factors. Important properties of the charge and weak form factors have also been discussed in the context of the Symmetrized Fermi Function and radius of the density distribution. The accuracy for experimental errors has been shown in order to constrain the theoretical models. Furthermore, the formalism for model-independent measurements of the radius of the density distributions and the weak skin radius have been formulated and the calculated radii have been represented in tabular form. Finally, the results for the CEνNS cross section and the importance of a precise measurement of the weak form factor have been discussed.

CHAPTER 4

CONCLUSION

The wide range of applicability of CEνNS in many disciplines in physics is of immense motivation to continue to further our knowledge of the subject. Of particular importance and the main motivation for this study, is the immense role that nuclear structure physics has played in furthering our understanding of the CEνNS cross-section. The weak form factor, being the last piece of physics for predictive capabilities of CEνNS, was calculated based on relativistic mean-field potentials. Using the given model-dependent, complex mean-field potentials for the interactions of the individual nucleons, the point-nuclear density distributions were constructed. It was shown that the structure of the point-nuclear density distributions near the origin was largely controlled by the energy scheme that the model predicted, namely the $l = 0$ occupied energy levels. Furthermore, due to the energy differences of the order of ≤ 1 MeV, the spectra for the same nuclei could differ between models. The structural differences of the density distribution between models were qualitatively described in terms of the surface diffuseness and half-density radius to describe the form factor—precise at large values of momentum transfer. It was shown that the half-density radius controls the form factor oscillations and the surface diffuseness was responsible for the exponential decay. Moreover, the exponential fall-off of the form factor could also be described by the size of the mean-squared radius to first order, where the larger radius of the density distribution would reflect larger exponential decay in the form factor expansion. The radius of the density distributions were also calculated for the various nuclei studied to show the model dependence and validate the predicted neutron distributions by comparing our results with the known proton radii. The neutron-rich nuclei with a larger radius gave much larger corrections to the CEνNS cross-section. Due to the extremely large corrections up to $\sim 40\%$ for Lead-208, the precise measurement of the weak form factors is necessary. Using the predicted weak form factors, the differential and total cross-sections were calculated. The relationship between

the enhancement to the cross-section due to the number of neutrons and the threshold for the nuclear recoil, a unique experimental limitation, was shown. Finally, the model-independent analysis that was formulated for the extraction of the radius of the density distributions and weak radius, as well as the precision needed to constrain the models could guide experiments that probe the weak interaction through CEνNS in the future.

REFERENCES

[1] K. Scholberg, "Observation of coherent elastic neutrino-nucleus scattering by coherent," *arXiv preprint arXiv:1801.05546*, 2018.

[2] N. Polukhina and N. Starkov, "New experiment for wimp direct search (newsdm)," *EPJ Web of Conferences*, vol. 191, p. 02023, 01 2018.

[3] S. Abrahamyan, Z. Ahmed, H. Albataineh, K. Aniol, D. S. Armstrong, W. Armstrong, T. Averett, B. Babineau, A. Barbieri, V. Bellini, R. Beminiwattha, J. Benesch, F. Benmokhtar, T. Bielarski, W. Boeglin, A. Camsonne, M. Canan, P. Carter, G. D. Cates, C. Chen, J.-P. Chen, O. Hen, F. Cusanno, M. M. Dalton, R. De Leo, K. de Jager, W. Deconinck, P. Decowski, X. Deng, A. Deur, D. Dutta, A. Etile, D. Flay, G. B. Franklin, M. Friend, S. Frullani, E. Fuchey, F. Garibaldi, E. Gasser, R. Gilman, A. Giusa, A. Glamazdin, J. Gomez, J. Grames, C. Gu, O. Hansen, J. Hansknecht, D. W. Higinbotham, R. S. Holmes, T. Holmstrom, C. J. Horowitz, J. Hoskins, J. Huang, C. E. Hyde, F. Itard, C.-M. Jen, E. Jensen, G. Jin, S. Johnston, A. Kelleher, K. Kliakhandler, P. M. King, S. Kowalski, K. S. Kumar, J. Leacock, J. Leckey, J. H. Lee, J. J. LeRose, R. Lindgren, N. Liyanage, N. Lubinsky, J. Mammei, F. Mammoliti, D. J. Margaziotis, P. Markowitz, A. McCreary, D. McNulty, L. Mercado, Z.-E. Meziani, R. W. Michaels, M. Mihovilovic, N. Muangma, C. Muñoz Camacho, S. Nanda, V. Nelyubin, N. Nuruzzaman, Y. Oh, A. Palmer, D. Parno, K. D. Paschke, S. K. Phillips, B. Poelker, R. Pomatsalyuk, M. Posik, A. J. R. Puckett, B. Quinn, A. Rakhman, P. E. Reimer, S. Riordan, P. Rogan, G. Ron, G. Russo, K. Saenboonruang, A. Saha, B. Sawatzky, A. Shahinyan, R. Silwal, S. Sirca, K. Slifer, P. Solvignon, P. A. Souder, M. L. Sperduto, R. Subedi, R. Suleiman, V. Sulkosky, C. M. Sutera, W. A. Tobias, W. Troth, G. M. Urciuoli, B. Waidyawansa, D. Wang, J. Wexler, R. Wilson, B. Wojtsekhowski, X. Yan, H. Yao, Y. Ye, Z. Ye, V. Yim, L. Zana, X. Zhan, J. Zhang, Y. Zhang, X. Zheng, and P. Zhu, "Measurement of the neutron radius of ^{208}pb through parity violation in electron scattering," *Phys. Rev. Lett.*, vol. 108, p. 112502, Mar 2012.

[4] F. Hasert, H. Faissner, W. Krenz, J. V. Krogh, D. Lanske, J. Morfin, K. Schultze, H. Weerts, G. Bertrand-Coremans, J. Lemonne, J. Sacton, W. V. Doninck, P. Vilain, C. Baltay, D. Cundy, D. Haidt, M. Jaffre, P. Musset, A. Pullia, S. Natali, J. Pattison, D. Perkins, A. Rousset, W. Venus, H. Wachsmuth, V. Brisson, B. Degrange, M. Haguenauer, L. Kluberg, U. Nguyen-Khac, P. Petiau, E. Bellotti, S. Bonetti, D. Cavalli, C. Conta, E. Fiorini, M. Rollier, B. Aubert, L. Chounet, P. Heusse, A. Lagarrigue, A. Lutz, J. Vialle, F. Bullock, M. Esten, T. Jones, J. McKenzie, A. Michette, G. Myatt, J. Pinfold, and W. Scott, "Search for elastic muon-neutrino electron scattering," *Physics Letters B*, vol. 46, no. 1, pp. 121 – 124, 1973.

[5] D. Z. Freedman, "Coherent effects of a weak neutral current," *Phys. Rev. D*, vol. 9, pp. 1389–1392, Mar 1974.

[6] D. Akimov, J. Albert, P. An, C. Awe, P. Barbeau, B. Becker, V. Belov, A. Brown, A. Bolozdynya, B. Cabrera-Palmer, *et al.*, "Observation of coherent elastic neutrino-nucleus scattering," *Science*, vol. 357, no. 6356, pp. 1123–1126, 2017.

[7] K. Scholberg, "Coherent elastic neutrino-nucleus scattering," in *Journal of Physics: Conference Series*, vol. 606, p. 012010, IOP Publishing, 2015.

[8] S. Bilenky, "Neutrino. history of a unique particle," *The European Physical Journal H*, vol. 38, pp. 345–404, Apr 2013.

[9] I. Angeli and K. Marinova, "Table of experimental nuclear ground state charge radii: An update," *Atomic Data and Nuclear Data Tables*, vol. 99, no. 1, pp. 69 – 95, 2013.

[10] L. Ray, W. R. Coker, and G. W. Hoffmann, "Uncertainties in neutron densities determined from analysis of 0.8 gev polarized proton scattering from nuclei," *Phys. Rev. C*, vol. 18, pp. 2641–2655, Dec 1978.

[11] V. E. Starodubsky and N. M. Hintz, "Extraction of neutron densities from elastic proton scattering by ^{206,207,208}Pb at 650 mev," *Phys. Rev. C*, vol. 49, pp. 2118–2135, Apr 1994.

[12] B. C. Clark, L. J. Kerr, and S. Hama, "Neutron densities from a global analysis of medium-energy proton-nucleus elastic scattering," *Phys. Rev. C*, vol. 67, p. 054605, May 2003.

[13] J. Zenihiro, H. Sakaguchi, S. Terashima, T. Uesaka, G. Hagen, M. Itoh, T. Murakami, Y. Nakatsugawa, T. Ohnishi, H. Sagawa, *et al.*, "Direct determination of the neutron skin thicknesses in ^{40,48}Ca from proton elastic scattering at $E_p = 295$ MeV," *arXiv preprint arXiv:1810.11796*, 2018.

[14] K. Patton, J. Engel, G. C. McLaughlin, and N. Schunck, "Neutrino-nucleus coherent scattering as a probe of neutron density distributions," *Phys. Rev. C*, vol. 86, p. 024612, Aug 2012.

[15] D. H. Beck and R. D. McKeown, "Parity-violating electron scattering and nucleon structure," *Annual Review of Nuclear and Particle Science*, vol. 51, no. 1, pp. 189–217, 2001.

[16] C. J. Horowitz, Z. Ahmed, C.-M. Jen, A. Rakhman, P. A. Souder, M. M. Dalton, N. Liyanage, K. D. Paschke, K. Saenboonruang, R. Silwal, G. B. Franklin, M. Friend, B. Quinn, K. S. Kumar, D. McNulty, L. Mercado, S. Riordan, J. Wexler, R. W. Michaels, and G. M. Urciuoli, "Weak charge form factor and radius of ^{208}pb through parity violation in electron scattering," *Phys. Rev. C*, vol. 85, p. 032501, Mar 2012.

[17] X. Roca-Maza, M. Centelles, X. Viñas, and M. Warda, "Neutron skin of ^{208}Pb, nuclear symmetry energy, and the parity radius experiment," *Phys. Rev. Lett.*, vol. 106, p. 252501, Jun 2011.

[18] K. M. Patton, G. C. Mclaughlin, and K. Scholberg, "Prospects for using coherent elastic neutrino-nucleus scattering to measure the nuclear neutron form factor," *International Journal of Modern Physics E*, vol. 22, no. 06, p. 1330013, 2013.

[19] J. Piekarewicz and M. Centelles, "Incompressibility of neutron-rich matter," *Phys. Rev. C*, vol. 79, p. 054311, May 2009.

[20] L.-W. Chen, C. M. Ko, and B.-A. Li, "Nuclear matter symmetry energy and the neutron skin thickness of heavy nuclei," *Phys. Rev. C*, vol. 72, p. 064309, Dec 2005.

[21] M. Centelles, X. Roca-Maza, X. Viñas, and M. Warda, "Nuclear symmetry energy probed by neutron skin thickness of nuclei," *Phys. Rev. Lett.*, vol. 102, p. 122502, Mar 2009.

[22] C. J. Horowitz and J. Piekarewicz, "Neutron star structure and the neutron radius of ^{208}*pb*," *Phys. Rev. Lett.*, vol. 86, pp. 5647–5650, Jun 2001.

[23] C. J. Horowitz and J. Piekarewicz, "Constraining urca cooling of neutron stars from the neutron radius of ^{208}Pb," *Phys. Rev. C*, vol. 66, p. 055803, Nov 2002.

[24] J. R. Wilson, "Coherent neutrino scattering and stellar collapse," *Phys. Rev. Lett.*, vol. 32, pp. 849–852, Apr 1974.

[25] K. Scholberg, "Supernova neutrino detection," *Annual Review of Nuclear and Particle Science*, vol. 62, no. 1, pp. 81–103, 2012.

[26] D. K. Papoulias and T. S. Kosmas, "Coherent constraints to conventional and exotic neutrino physics," *Phys. Rev. D*, vol. 97, p. 033003, Feb 2018.

[27] A. A. Aguilar-Arevalo, B. C. Brown, L. Bugel, G. Cheng, E. D. Church, J. M. Conrad, R. Dharmapalan, Z. Djurcic, D. A. Finley, R. Ford, F. G. Garcia, G. T. Garvey, J. Grange, W. Huelsnitz, C. Ignarra, R. Imlay, R. A. Johnson, G. Karagiorgi, T. Katori, T. Kobilarcik, W. C. Louis, C. Mariani, W. Marsh, G. B. Mills, J. Mirabal, C. D. Moore, J. Mousseau, P. Nienaber, B. Osmanov, Z. Pavlovic, D. Perevalov, C. C. Polly, H. Ray, B. P. Roe, A. D. Russell, M. H. Shaevitz, J. Spitz, I. Stancu, R. Tayloe, R. G. Van de Water, D. H. White, D. A. Wickremasinghe, G. P. Zeller, and E. D. Zimmerman, "Improved search for $\overline{\nu}_\mu \to \overline{\nu}_e$ oscillations in the miniboone experiment," *Phys. Rev. Lett.*, vol. 110, p. 161801, Apr 2013.

[28] J. Billard, E. Figueroa-Feliciano, and L. Strigari, "Implication of neutrino backgrounds on the reach of next generation dark matter direct detection experiments," *Phys. Rev. D*, vol. 89, p. 023524, Jan 2014.

[29] I. J. R. Aitchison and A. J. G. Hey, *Gauge theories in particle physics : a practical introduction.* Graduate student series in physics, Institute of Physics Pub., 2003.

[30] D. J. Griffiths, *Introduction to elementary particles.* Wiley-VCH, 2004.

[31] C. J. Horowitz and J. Piekarewicz, "Impact of spin-orbit currents on the electroweak skin of neutron-rich nuclei," *Phys. Rev. C*, vol. 86, p. 045503, Oct 2012.

[32] Z. Ye, J. Arrington, R. J. Hill, and G. Lee, "Proton and neutron electromagnetic form factors and uncertainties," *Physics Letters B*, vol. 777, pp. 8 – 15, 2018.

[33] B. G. Todd and J. Piekarewicz, "Relativistic mean-field study of neutron-rich nuclei," *Phys. Rev. C*, vol. 67, p. 044317, Apr 2003.

[34] H. Müller and B. D. Serot, "Relativistic mean-field theory and the high-density nuclear equation of state," *Nuclear Physics A*, vol. 606, no. 3, pp. 508 – 537, 1996.

[35] R. Utama, W.-C. Chen, and J. Piekarewicz, "Nuclear charge radii: density functional theory meets bayesian neural networks," *Journal of Physics G: Nuclear and Particle Physics*, vol. 43, p. 114002, oct 2016.

[36] J. J. Sakurai, *Advanced quantum mechanics.* Addison-Wesley Pub. Co., 1987.

[37] M. Schumann, "Dark matter search with liquid noble gases," *arXiv preprint arXiv:1206.2169*, 2012.

[38] J. Piekarewicz, A. R. Linero, P. Giuliani, and E. Chicken, "Power of two: Assessing the impact of a second measurement of the weak-charge form factor of ^{208}Pb," *Phys. Rev. C*, vol. 94, p. 034316, Sep 2016.

BIOGRAPHICAL SKETCH

Jesse António Hernández was born on June 10, 1994, on Long Island, New York. He attended Valley Stream South High School for early education where he graduated with honors in 2012. Following graduation, he was admitted and attended the State University of New York (SUNY) at Buffalo as a Bachelors of Science (B.Sc.) in physics. In 2016, he graduated from SUNY Buffalo with his B.Sc. in physics and a minor in mathematics. Following graduation from SUNY Buffalo, he attained a job tutoring students of introductory college classes in mathematics and physics while simultaneously applying to graduate programs in physics. In the summer of 2017, he was accepted as a graduate student at Florida State University (FSU) as a bridge student. At FSU he researched theoretical nuclear physics culminating in a successful Masters Thesis defense. In the Fall of 2019, he will be awarded his Masters of Science (M.Sc.) degree from FSU. He will continue in physics by pursuing his Doctor of Philosophy (Ph.D.) degree at FSU.